Time-resolved oxidative signal convergence across the algae–embryophyte divide

Tim P. Rieseberg[1,*,#],Armin Dadras[1,*], Tatyana Darienko[1], Sina Post[2], Cornelia Herrfurth[2,3], Janine M. R. Fürst-Jansen[1], Nils Hohnhorst[1], Romy Petroll[4], Stefan A. Rensing[5], Thomas Pröschold[1,6], Sophie de Vries[1], Iker Irisarri[1,7,8], Ivo Feussner[2,3,9], Jan de Vries[1,2,7,10#]

1 — University of Goettingen, Institute of Microbiology and Genetics, Department of Applied Bioinformatics, Goldschmidtstr. 1, 37077 Goettingen, Germany
2 — University of Goettingen, Albrecht Haller Institute of Plant Science, Department of Plant Biochemistry, Justus-von-Liebig-Weg, 37077 Goettingen, Germany
3 — University of Goettingen, Goettingen Center for Molecular Biosciences (GZMB), Service Unit for Goettingen Metabolomics and Lipidomics, Justus-von-Liebig Weg 11, 37077 Goettingen, Germany
4 — Department of Algal Development and Evolution, Max Planck Institute for Biology Tübingen, Tübingen, Germany
5 — University of Freiburg, Centre for Biological Signalling Studies (BIOSS), Freiburg, Germany
6 — University of Innsbruck, Research Department for Limnology, 5310 Mondsee, Austria
7 — University of Goettingen, Campus Institute Data Science (CIDAS), Goldschmidtstr. 1, 37077 Goettingen, Germany
8 — Section Phylogenomics, Centre for Molecular Biodiversity Research, Leibniz Institute for the Analysis of Biodiversity Change (LIB), Museum of Nature, Hamburg, Martin-Luther-King Platz 3, 20146 Hamburg, Germany
9 — University of Goettingen, Goettingen Center for Molecular Biosciences (GZMB), Department of Plant Biochemistry, Justus- von-Liebig Weg 11, 37077 Goettingen, Germany
10 — University of Goettingen, Goettingen Center for Molecular Biosciences (GZMB), Department of Applied Bioinformatics, Goldschmidtstr. 1, 37077 Goettingen, Germany
*contributed equally
#authors for correspondence: timphilipp.rieseberg@uni-goettingen.de & devries.jan@uni-goettingen.de

ORCID: Tim P Rieseberg 0000-0003-3548-8475, Armin Dadras 0000-0001-7649-2388, Janine MR Fürst-Jansen 0000-0002-5269-8725, Tatyana Darienko 0000-0002-1957-0076, Cornelia Herrfurth: 0000-0001-8255-3255, Ivo Feussner: 0000-0002-9888-7003, Iker Irisarri 0000-0002-3628-1137, Stefan A. Rensing 0000-0002-0225-873X, Thomas Pröschold 0000-0002-7858-0434, Sophie de Vries 0000-0002-5267-8935, Jan de Vries 0000-0003-3507-5195

ABSTRACT

The earliest land plants faced a significant challenge in adapting to environmental stressors. Stress on land is unique in its dynamics, entailing swift and drastic changes in light and temperature. While we know that land plants share with their closest streptophyte algal relatives key components of the genetic makeup for dynamic stress responses, their concerted action is little understood. Here, we combined time-course stress profiling using photophysiology, transcriptomics on 2.7 Tbp of data, and metabolite profiling analyses on more than 270 distinct samples, to study stress kinetics across three 600-million-year-divergent streptophytes. Through co-expression analysis and Granger causal inference we predict a gene regulatory network that retraces a web of ancient signal convergence at ethylene signaling components, osmosensors, and chains of major kinases. These kinase hubs already integrated diverse environmental inputs since before the dawn of plants on land.

INTRODUCTION

Earth's surface teems with photosynthesizing life. Biodiverse cyanobacteria and algae form green biofilms on rocks and tree bark, and lichens thrive on the bleakest mountaintops. All of this is however dwarfed by the lineage that conquered land globally: the land plants (embryophytes)[1]. Together with streptophyte algae, land plants belong to the streptophytes[2]. Phylogenomic analyses established that the Zygnematophyceae are the closest streptophyte algal relatives of land plants[2-4] and comparative genomics have ushered in major progress in establishing a shared catalogue of traits between streptophyte algae and land plants[5-10]. Yet, we are only beginning to understand how these genes might have been used in a functional advantage at the time of the conquest of land[11]. Several synergistic properties have shaped land conquering plants[12], including multicellular development[13,14], propagation[15], symbiosis[16,17], and stress response[18]. In case of the latter, the earliest land plants had to overcome a diverse range of stressors to which modern land plants dynamically respond by adjusting their growth and physiology[19]. One of the hallmarks of abiotic stress on land in contrast to water is its more dynamic nature: life on land involves rapid and drastic shifts in temperature, light or water availability[18]. We focus on two terrestrial stressors — strongly fluctuating temperatures (cold and heat stress) and light conditions (high light stress and recovery).

Terrestrial stressors impact plant and algal physiology especially through the generation of reactive oxygen species (ROS) in the plastid; the plastid acts as a signaling hub upon environmental challenge[20-22]. Carotenoids are integral in the oxidative stress mitigation networks of Chloroplastida

and found in nearly any photosynthetic organism[23,24]. By quenching oxidative stress of different nature, oxidative breakdown products of the polyene backbone called apocarotenoids are a consequence[25,26]. Apocarotenoids act as signals in attuning plant and plastid physiology to stress[27-31]. The diversity of apocarotenoids is vast, including land plant hormones like abscisic acid (ABA)[32,33] and strigolactones[34] but also small volatiles like β-ionone (β-IO) and β-cyclocitral (β-CC) with a growing number of recognized functions[27-31,35]. The involvement of β-CC in high light stress response was confirmed by several studies in *Arabidopsis thaliana*[27,29] and some data also suggests a role in retrograde signaling[36,37]. A physicochemical consequence of the elevation of atmospheric oxygen levels due to plant terrestrialization and radiation[38] might have been higher rates in apocarotenogenesis— independent of the evolution of carotenoid-cleaving enzymes. The utilization of signals derived from carotenoids in the first land plants is hence plausible and adaptive.

Here, we studied the integration of apocarotenoid signals and oxidative stress networks in three genome-sequenced non-vascular streptophytes: the algae *Zygnema circumcarinatum*[10] and *Mesotaenium endlicherianum*[7,11], and the land plant *Physcomitrium patens*[39]. Data on pigment profiles and photophysiology were correlated with time-resolved global gene expression profiles from more than 270 samples in total. Using co-expression and gene regulatory network inference, we retrace a web of ancient kinase hubs where environmental and apocarotenoid signals converged already in the last common ancestor of embryophytes and algae.

RESULTS

A comparative framework for stress dynamics across 600 million years of streptophyte evolution

We worked with three genome-sequenced streptophytes that are 600-million-years-divergent (Fig. 1a) under comparable conditions (see Methods; briefly, 20/25 °C, 80–100 µmol photons m^{-2} s^{-1}): two representatives of the diverse and species-rich[40] closest algal relatives of land plants, the filamentous alga *Zygnema circumcarinatum*[10] SAG 698-1b (henceforth *Zc*) and the unicellular alga *Mesotaenium endlicherianum*[7,11] SAG 12.97 (*Me*) and the bryophyte model *Physcomitrium patens*[39] strain Gransden 2004 (*Pp*). After growth to apt density, we challenged the organisms by shifting them to (i) high light stress (HL) at 10x growth light intensity (i.e., 800-1050 µmol photons m^{-2} s^{-1}) for 6h followed by (ii) 4h of recovery at standard growth conditions, and 24h of (iii) low temperature at 12 °C colder and (iv) high temperature at 12 °C warmer than standard growth condition; all experimentation was repeated in three successive biological replicates (Fig. 1b). To track the physiological response of the three streptophytes, we measured their relative photosynthetic yield (Fq'/Fm') using pulse-amplitude-modulation (PAM) fluorometry (Fig. 1c-e) at 13 time points (Fig. 1b).

On balance, responses upon stress were well conserved in the three studied organisms but acted in slightly differing kinetics (Fig. 1c). HL brought the swiftest changes in Fq'/Fm' (Fig. 1e), with an average drop by 0.49±0.08 at 30 min (Fig. 1c). While *Me* and *Pp* recovered progressively after HL, *Zc* gusted to the initial values but recovered later (Fig. 1c). In all three studied species HL caused a stronger and faster response in Fq'/Fm' than temperature stress (Fig. 1c). In *Zc* and *Me* the stressors additionally induced morphological alterations (Fig. 1f)—in both causing significant changes in chloroplast shape upon HL and heat as well as LD accumulation upon cold (Fig. 1g); in *Zc*, heat and HL further induced pigment alterations and plasmolysis (Fig. 1g).

Overall, our setup captures quantifiable changes in physiology that follow a stress kinetic. We next turned to the molecular consequences.

Global transcriptomics bear out divergent time-course dynamics

To understand how the temporal and amplitudinal differences in physiology relate to genetic changes, we used global gene expression analysis. We generated RNA-seq data on samples from 29 different conditions in biological triplicates (sextuplicates for t_0) across all three species, yielding a total of 270 samples. All sequencing was performed on the NovaSeq6000 platform (Illumina) using paired-end 150 bp reads, yielding 2.8 Tbp (2,806,144,787,400 bp), of which 2.7 Tbp were retained after quality filtering (2,710,780,974,000 bp). We mapped the data onto the respective genomes based on current gene models[10,11,39] with an average alignment rate of 83.39%, 67.39%, and 92.58 % for *Me*, *Zc*, and *Pp*, respectively. A principal component analysis (PCA) of gene expression data recovered a clear separation between stress and control conditions (Fig. 2a). Along PC1 (describing between 26.9% to 44% of the variance; Fig. 2a) heat followed by HL showed the swiftest separation upon temporal

progression in all three streptophytes (Fig. 2b); recovery caused time-successive rapprochement to control conditions (Fig. 2a). Treatment with cold generally induced less differences from control conditions and resembled characteristics of a resting state despite slight fluctuations likely due to circadian rhythms.

To pinpoint the functions that underpin the temporal dynamics of stress response, we performed differential gene expression analysis of each treatment to its respective control. We carried out 22 comparisons for each species (Extended Data Fig. 1a), yielding up to more than 3000 significantly differentially expressed genes (Extended Data Fig. 1b), and performed GO term enrichment across time and treatments (Fig. 2c). HL induces rapid responses whereas responses to cold were more delayed except in *Me*. In general, *Me* showed the highest responsiveness towards the studied environmental cues (Extended Data Fig. 1b). Further, on balance, *Zc* showed the most delayed response (Fig. 2c)—even in the recovery (Extended Data Fig. 2). Recurrent themes corroborated previous findings[11,41]: among the responses, light quality signaling, response to ROS, and chloroplast as well as photosynthesis-associated processes stuck out (Extended Data Fig. 3). In *Me* calcium and kinases featured prominently in the temperature stresses (Fig. 2c). Overall, the gene expression data align with the physiological data. We next turned to a physiological stress mitigation mechanism that generates signals: carotenoid metabolism and apocarotenoid signals.

Dynamic xanthophyll cycle and apocarotenogenesis in *Mesotaenium*

Under stress, carotenoid levels adjust and yield apocarotenoid signals through oxidative cleavage[23] (Fig. 3a). To assess their profiles, we combined RP-C_{30}-HPLC-UV-Vis (carotenoids and chlorophylls) with HS-SPME-GC-MS (volatile apocarotenoids; Fig. 3b,c,e) and investigated transcript levels of relevant genes (Fig. 3d). In general, pigment fluctuations due to stress exposure seem more similar in the two studied multicellular organisms than in the unicellular *Me* (Fig. 3b,c,e); for example, the de-epoxidation state changed after 15 minutes of HL by 1.98-fold in *Me*, 1.09-fold in *Zc*, and 1.35-fold in *Pp*. Changes in the relative xanthophyll pool size were ±20% upon 2 h of treatment by any stressor relative to t_0 (Fig. 3c), suggesting that the overall response is mainly determined by the altered physicochemical stress conditions. This is also reflected by transcript level changes in homologs of enzymes responsible for gross flux regulation (Fig. 3d). Since enzymatic reactions of the carotenoid pathway are favored by heat and other biosynthetic steps are favored by light in both conditions, transcript levels of these enzymes, including homologs of PDS, CRTISO, CYP97A, are downregulated: for example, after 6 h PDS was downregulated—relative to control—in *Me* 44-fold (heat) and 13.5-fold (HL) (BH-corrected $P = 1.28\text{x}10^{-17}$ and $1.52\ \text{x}10^{-11}$), and in *Zc* downregulated by 2.4-fold (heat) and 1.6-fold (HL) (BH-corrected $P = 7.64\text{x}10^{-6}$ and 0.016); in *Pp* PDS expression did not change or was upregulated by 3.2-fold under cold (BH-corrected $P = 8.68\text{x}10^{-12}$; Fig. 3e). The pigment pools of *Me* and *Pp* are of similar sizes (compared to *Pp*, t_0 95% and 100%) while *Zc* has a much smaller pool (13%; Fig. 3c). An explanation is that the weight of mucilage skews the values for *Zc*. The pigment pool of *Me* was the most dynamic (Fig. 3c,e). The ratio of β-carotene to the apocarotenoids β-CC, β-IO, and dihydroactinidiolide (DHA) had changed after 2h of treatment most pronouncedly upon HL, down to 0.36, 0.59, and 0.31 for *Me*, *Zc*, and *Pp* compared to 1.05, 0.59, and 0.41 in cold and 0.35, 0.9, and 0.65 upon heat (Fig. 3b,e). As expected, there was no direct correlation between changes in apocarotenoid levels and transcript levels, because apocarotenoids are also formed by non-enzymatic cleavage. The non-enzymatic cleavage reaction is favored under elevated temperatures and HL and we observe decreasing transcript levels: in *Me* and *Pp*, CCD1 showed the most dynamic in the first 2h of treatment, decreasing 3.3- and 5.5-fold in *Me* upon heat and HL (BH-corrected $P = 7.63\text{x}10^{-7}$ and $8.05\text{x}10^{-13}$) and 3.9-fold in *Pp* upon heat (BH-corrected $P = 1.56\text{x}10^{-15}$). Me*CCD1* constantly rose during the first 6h cold stress up to 6.4-fold (BH-corrected $P = 1.12\text{x}10^{-11}$), while β-CC, β-IO levels reached their peak at 4h cold. β-IO appears to be swiftly converted to DHA in a non-enzymatic reaction[26,27]. DHA has also shown a stronger effect on oxidative stress-responsive genes in earlier studies[27,42]. Overall, we recovered the presence of well-known apocarotenoid signals with the most pronounced stress kinetics in *Mesotaenium*.

Biological programs correlate with the environmental triggers and pigment profiles

Each organism reacted to the environmental cues by the altered expression of up to thousands of genes. To understand their cooperative action, we clustered all 13125, 9445, and 15778 genes that passed the expression cutoff in *Me*, *Zc*, and *Pp* into 27, 34, and 29 clusters respectively, to which we

refer by color (Fig. 4a). We then asked the questions of how these clusters (i) correlate with the environmental cues and apocarotenoid levels (Fig. 4b) and (ii) are similar across species (Fig. 4c,d). For the latter, we worked with Orthofinder's hierarchical orthogroups (HOGs) and calculated the Jaccard distance (Fig. 4c,d).

The gene clusters consist of meaningful biological cohorts, such as *Me*darkred and *Pp*darkgrey that are similar (Fig. 4d) and enriched in ribosomal GO-terms, and ribosome component-coding genes that are hubs in these networks (Extended Data Figs. 4 and 5). Physiologically coherent behaviors were recovered. For example, cluster *Me*yellow shows negative correlation with temperature (r = −0.73, $P = 10^{-13}$) and the ratios of antheraxanthin (A) + zeaxanthin (Z) to violaxanthin (V) + A + Z (AZ/VAZ) (r = −0.52, $P = 2\text{x}10^{-6}$), with the similar cluster *Pp*yellow showing a negative correlation with temperature (r = −0.67, $P = 10^{-10}$) and similar terms associated with (Fig 4c; Extended Data Fig. 5); in contrast, for example, *Me*darkorange showed weak correlation with temperature (r = 0.35, P = 0.003) and light intensity (r = 0.33, P = 0.006; Extended Data Fig. 5). Clusters of *Zc* seldom showed correlations with the tested environmental factors but this is likely due to *Zc*'s subdued responses. Overall, the clearest correlations were with temperature, where highly similar clusters (Fig. 4c,d) such as *Me*brown (Fig. 4e), *Pp*brown (Fig. 4f), *Zc*brown (Extended Data Fig. 5), and *Me*Turquoise (Fig. 4g) show strong positive correlations (r = 0.85, $P = 5\text{x}10^{-23}$; r = 0.64, $P = 10^{-9}$; r = 0.74, $P = 2\text{x}10^{-13}$; and r = 0.39, $P = 7\text{x}10^{-4}$) and similar terms associated with protein homeostasis.

Several clusters reflect signaling processes, including kinases and HISTIDINE KINASE (AHK) hubs (Fig. 4f,h,i,j; Extended Data Fig. 5), calcium and Ca^{2+}-DEPENDENT KINASE (CDPK) hubs (Fig. 4i), photomorphogenesis (Fig. 4g), and links of kinases and carotenogenesis (Fig. 4f). The clearest correlation with the apocarotenoid signals showed *Pp*pink and *Me*black (r = 0.61, $P = 10^{-8}$ and r = 0.41, $P = 3\text{x}10^{-4}$). *Pp*pink was enriched in light intensity including the phytochrome signaling hub LONG AFTER FAR-RED 3 (LAF3)[43] and oxidoreductase activity including a superoxide dismutase hub (Extended Data Fig. 5). *Me*black showed a very complex and broad enrichment of genes associated with general transcription processes. To disentangle these genetic networks, we next used temporal clustering.

Temporal stress co-expression and Granger causal inference of gene regulatory networks

To understand the time-course dynamics of the responses, we modeled clusters of gene expression along their time course using a Dirichlet process Gaussian process mixture model[44] (DPGP). Using DPGP, we clustered all 11670, 9781, and 3887 genes that passed the expression cutoff in *Me*, *Zc*, and *Pp* into 12 to 16, 13 to 20, and 11 to 13 clusters. We filtered these clusters, retaining only those that had a Gaussian probability of at least 0.7 and calculated their Jaccard distances (Fig. 5a). As expected, the most similar clusters occurred within a species. However, there were several similar clusters across species, including a cohort of genes downregulated upon heat in *Pp*C6 and *Me*C3 related to photosynthesis (Fig. 5b).

We next turned to understand how the hubs of the co-expression clusters identified via WGCNA behave along the temporal gradient, with a focus on signaling hubs. Hub genes show focal occurrence among DPGP clusters. For example, hubs of *Me*yellow (chloroplast and photosynthesis; Extended Data Fig. 5d) were mainly in cohort of early down-regulated genes upon HL *Me*C1 (Fig. 5c); *Pp*yellow showed a similar behavior (Fig. 5c). Early upregulated hubs included those of protein homeostasis in *Me*brown.

Research on model land plants has established a rich framework of genetic cascades that act in information processing and are structured a hierarchy. To understand how the temporal expression behaviors of the genes are linked in the 600-million-year divergent streptophytes, we predicted gene regulatory relationships based on Granger causality using Sliding Window Inference for Network Generation (SWING) and a Random Forrest (RF) approach (i.e., SWING-RF)[45]. For this, we worked with a subset of 1897, 3694, and 1629 genes and 24 metabolite levels and ratios in *Me*, *Zc*, and *Pp*, predicting 375,273 to 3,358,660 non-zero interactions between genes (and metabolites), yielding putative gene regulatory networks (GRNs; Extended Data Fig. 7). We then asked the question of how the genes that group into HOGs and show conserved behavior in DPGP clusters predict each other (Fig. 6a,b) and recovered a network of 923 conserved gene pairs (1239, 1188, and 1369 in *Me*, *Zc*, *Pp*); in addition, we also investigated the topology of the network if we (i) group genes simply using best BLAST hits (BBH; Extended Data Fig. 8), recovering a network of 757 conserved genes, and (ii) re-compute the network using all time points of stress treatment—also those for which no metabolite

data were generated, recovering a network of 900 (Extended Data Fig. 9). The topology of the predicted GRN highlighted several major points of convergence—hubs (Fig. 6c,d).

Physical feedback

Mechanosensitive channels, regulate ion flow in response to mechanical cues. We recover protein homologs from the OSCA family, calcium-permeable channels sensitive to hyperosmolality[46], as highly connected points of convergence (Fig. 6a,c,d). Feeding into them was a PDS1-PDS3 network (Fig. 6), genes with highly responsive expression change under stress (Fig. 3d), underpinning a central link of carotenogenesis to all kinds of oxidative stress responses. Connected genes included those with general functions such as homologs of CYTOSOLIC IRON-SULFUR PROTEIN ASSEMBLY 1 (CIA) but also SOUL homologs (Fig. 6a). SOUL are heme-binding proteins[47] that can translocate to the chloroplast and are key for oxidative homeostasis[48].

Directly influenced by the OSCA hub was a large HOG of subtilases, which are known growth regulators[49,50]. Indeed, highly predictive for this subtilase hubs were a CXE HOG that also contained the growth regulating gibberellin receptor GIBBERELLIN INSENSITIVE DWARF1 (GID1)[51]—some *Me* homologs even bearing a homologous region to the unique n-terminal extension of GID1—and AHK1, which if interpreted as cytokinin-relevant, also speaks of ancient developmental programs. Indeed, upstream of CXE/GID was a HOG of GROWTH-REGULATING FACTORs (GFR). This speaks for a feedback of osmo-sensing—as done by OSCA and AHKs[52,53]—and growth programs in which subtilases are a point of convergence.

Convergence at ethylene programs

Ethylene signaling stands as the sole example of a phytohormone with a clear signaling cascade reported to be functionally conserved between land plants and Zygnematophyceae, although its biosynthetic pathway may not need to be necessarily conserved[54,55]. Exogenous ethylene treatment of the zygnematophyceaen alga *Spirogyra* induces growth phenotypes and the differential expression of stress- and photosynthesis-associated genes identified in land plants[56]. Crucially, *Spirogyra* homologs complement knockout lines in *Arabidopsis* ethylene signaling[57]. Ethylene thus both completes the stress and photosynthesis response cycle and represents the phytohormone with the most evident data supporting its conserved functional role in stress response in both land plants and Zygnematophyceae.

Our predicted GRN recovers several signature genes from ethylene signaling. We recover an ETR among the most highly connected homologs (Fig. 6c,d) and HOGs. Both in *Arabidopsis* and *Pp*, ethylene is detected by a two-component histidine kinase receptor subfamily of ETR1 homologs[58,59]. Upstream were meaningful regulatory cassettes including a HOG of Kelch repeat F-Box that includes homologs of the stress response and specialized metabolism regulators SMALL AND GLOSSY LEAVES (SAGL1)[60,61] and ATTENUATED FAR-RED RESPONSE (AFR)[62]. Indeed, further upstream were C2H2 zinc-finger TFs—TFs generally prominent in our SWING network—including SUF4, YY1 and are well known to be among the apocarotenoid-activated TF families[28,37,63], CONSTANS-like B-box TFs that include the CCT domain involved in light-dependent regulation[64-66], and phytochromes in line with their essential role in stress, light signaling, and several phytochrome signatures in our transcriptomes. And upstream of this is a HOG of various APETALA2 (AP2) TFs that include homologs of Ethylene Response Factors (ERFs) but have diverse functions in environmental and hormonal responses[67]. That said, in *Pp*, an ETR kinases play a crucial role in facilitating effective environmental stress responses through ethylene-mediated submergence signaling and ABA-mediated osmo-stress signaling[68]; our work adds in the conservation in the two Zygnematophyceae (Fig. 6). A HOG that includes the heat stress-relevant ARABIDOPSIS HOMOLOG OF TRITHORAX 1 and 2 (ATX)[69] was downstream, providing the single broker that linked it to the most connected hub in the predicted GRN: a kinase.

Environmental and apocarotenoid input converges at hubs of the kinome

In land plants, a network of kinases regulates responses to environmental input by phosphorylating proteins like TFs and enzymes, impacting synthesis of specialized metabolites, gene activation, and more[70-72]. Several factors modulate the activity of these kinases, including protein phosphatases acting as mediators but also direct signals if linked to a sensor, affecting response dynamics and outcomes. These kinases form converging points in our predicted GRN. They are the receivers of diverse inputs, integrating environmental input in biological programs.

As the single most connected receiver in our DPGP-filtered SWING-inferred GRN was an HOG of serine / threonine kinases (SPS; Fig. 6a-d), which include several receptor-like kinases[73]. In our analyses, these receive input from the apocarotenoid ß-IO and SUPPRESSOR OF FRIGIDA (SUF4), a putative zinc-finger-containing TF, regulating for delayed flowering in winter-annual *Arabidopsis* by suppressing the late-flowering FRI mutants through reduced H3K4 trimethylation at FLC; recently it was shown that SUF4 acts as a thermosensor, showing thermo-sensitive assembly and thus activity[74]. This warrants attention, as we recovered in the BBH-based analysis a whole putative regulatory chain of ß-IO–SUF4–a transmembrane protein–MYB4R1 (Extended Data Fig. 8). Furthermore, a HOG including the circadian regulators[75] LUX ARRHYTHMO (LUX) and BROTHER OF LUX ARRHYTHMO, were the fifth most predictive (Fig. 6d) on the SPS kinase hub expression behavior, aligning with their previously noted importance in photomorphogenesis co-expression hubs in *Mesotaenium*[11].

Around this SPS hub we recovered several genes that are known to be major hubs in regulation themselves. This included TOR, eukaryote-wide regulators of diverse developmental and metabolic processes[76,77], which are part of the kinase network. As potential regulator of the major kinase hub, a hub of PP2A B subunits appeared. This aligns with the regulatory subunit determining activation of the phosphatase complex and various subfamilies interact with different kinases[78].

Next to the major hub of SPS kinases, other kinase HOGs included AHKs. AHKs are best known as cytokinin signaling components[79] but also include respond to diverse abiotic stressors[52,53]. These AHKs form another hub upstream of the major SPS hub. As highlighted by the previous environmental gradient analysis on *Mesotaenium*[11] alone, we find chains of kinases (BSK, SERK, MKK) linked with a large group of EXORDIUM-like proteins, which are modulators of cell expansion[80] and thus likely the downstream target that modifies growth upon environmental input. These EXORDIUM-likes are connected via a mTERF4-like HOG to the central kinome (Fig. 6). mTERF transcription termination factors harbor many important functions in regulating organellar gene expression[81,82] and mTERF4 interplaying with GUN1 (see also *Zc*darkgreen, Extended Data Fig. 5) that is implicated in retrograde signaling[83].

Overall, the kinases form a major track throughout the entire GRN. Many of the kinases recovered are homologous to well-known integrators of environmental cues, via intracellular signaling, to growth and acclimation programs.

DISCUSSION

The success of the earliest land plants likely hinged on their capacity to perceive and react to environmental conditions. These environmental conditions are integrated into a network that bundles information and triggers developmental plasticity. Integrated in this web are key links between plastid and cell physiology: carotenoids and the signals they give rise to due to oxidative cleavage. Carotenoids are among the best conserved and most ancient oxidative stress-mitigating molecules in photosynthetic organisms[24,84]. With the synthesis of the first carotenoid non-enzymatically formed apocarotenoids were born – enzymes for controlled oxidative cleavage of the polyene backbone likely evolved later. Our data shows that apocarotenogenesis driven by physicochemical conditions is shared. What diversified were the genetic hubs and enzymes acting on them and controlling the formation and response likely favorable for terrestrialization—a process that came with more oxidative force and as a physicochemical consequence more apocarotenogenesis due to elevated O_2 levels, reduced CO_2 levels, a drastic drop in temperature and generally more abiotic stress due to terrestrial environmental conditions. We found several of these stress-mitigation hubs conserved in the two investigated Zygnematophyceae and the moss *P. patens*.

Traits of land plants are under an adaptability-driven selection since their emergence—and in many cases these signature genes emerged prior to the origin of land plants. Our findings pinpoint the hubs in which this information is bundled. Largely mediated by kinases that are known to integrate in signaling cascades that facilitate cross-talk between different inputs, for example bundling signaling molecules, Ca^{2+}, and osmotic[53,85], and their link to developmental programs. These kinases span a web, serving as points of convergence between inputs and redistribute these on the level of protein phosphorylation to the respective output. We here found that environmental programs regulate the transcriptional level across 600-million-year divergent streptophytes.

MATERIALS AND METHODS

Algae and moss cultivation

Mesotaenium endlicherianum SAG 12.97 and *Zygnema circumcarinatum* SAG 698-1b were obtained from the Culture Collection of Algae at Göttingen University (SAG) and grown on cellophane disks (folia®, Max Bringmann KG) as described[86] prior to stress treatment with the exception that in both cases agarized (1%) Woods Hole Medium (WHM)[87] was used. In short, fully-grown plates of stock cultures were suspended and inoculated on fresh WHM plates. *Mesotaenium endlicherianum* SAG 12.97 was grown for 8 d at 20 ± 1 °C with 80–90 µmol photons m^{-2} s^{-1} (Niello® LED 300 W, 380–740 nm spectrum; Suppl. Fig. 1) under 16/8-h light/dark cycle. *Zygnema circumcarinatum* SAG 698-1b was grown for 48 h at 20 ± 1 °C with 20–25 µmol photons m^{-2} s^{-1} (Niello® LED 300 W, 380–740 nm spectrum) and afterward for 11 d at 20 ± 1 °C with 80–90 µmol photons m^{-2} s^{-1} with the same 16/8-h light/dark cycle (13 d of total growth until the start of the experiment).

Physcomitrium patens Gransden 2004 strain 40001 protonema was used for the experiments. Agarized (0.55 %) basal minimum medium with ammonium tartrate (BCD-AT)[88] was used and inoculated with 2 mL of a suspension of the stock culture (one fully-grown plate per 20 mL sterile tab water) homogenized with an IKA® ULTRA-TURRAX®. Cultures were kept at 25 ± 1 °C during the light phase with 100 µmol photons m^{-2} s^{-1} (growth chambers of Percival Scientific, Inc., Perry, IA, USA) and at 18 ± 1 °C during dark phase under 16/8-h light/dark cycle for 7 d prior to stress treatment or sub-cultivation.

Stress treatments

Time-series stress experiments were performed as visualized in Fig. 1b in biological triplicates. Transcriptome and metabolite samples were harvested at the time points indicated by rectangular lines in Fig. 1b. Also, relative quantum yield was measured at these time points (for details see the photophysiological measurements section).

For the control timeline, cultures stayed for another 24 h at the cultivation conditions described above. For temperature stress treatments control light conditions were used but the temperature was 12 °C lower (cold stress) or higher (heat stress). Due to the reduced efficiency of the LEDs at elevated temperature, the light intensity dropped by 10 µmol photons m^{-2} s^{-1} during algae heat stress experiments (not the case for *Physcomitrium patens*).

Algae temperature stress treatments were performed in HS80 growth tents (Secret Jardin, Manage, Belgium) in temperature-controlled rooms. To ensure homogeneous temperature in the tents, cultures were put on an elevated grid and two small Clip-Fans (Garden Highpro Clip-Ventilator Ø15cm, 5 Watt) were added. *Physcomitrium patens* temperature stress series were performed in the Percival's with altered temperature programs.

For HL treatments cultures were transferred to a 10x light intensity regime compared to control conditions 800–900 µmol photons m^{-2} s^{-1} (algae) and 950–1050 µmol photons m^{-2} s^{-1} (moss) respectively, and afterwards 4 h to control conditions for recovery. In the case of algae high light treatments, the increased light intensity also led to a rise in temperature by 12 °C. The temperature stayed constant during *Physcomitrium patens* HL treatments.

To achieve this light intensity two lamps with higher output (Niello® LED 900 W, 380–740 nm spectrum) were used in the case of the algae treatments and for *Physcomitrium patens* HL treatments, 4 additional lamps (Niello® LED 300 W, 380–740 nm spectrum) were installed in the Percival.

Harvesting and storage of transcriptome and metabolite samples

Samples for transcriptomic analysis and metabolite profiling were harvested with a spatula at the respective timepoints and immediately frozen in liquid N_2 in reaction vials. Afterwards, samples were stored at –70 or –80 °C and metabolite samples additionally overlaid with argon before storage. To ensure a higher reproducibility, each transcriptome and metabolite sample was pooled from three different algae or moss plates (technical triplicate) at each timepoint. This was done in biological triplicates as described above.

Photophysiological measurements

Fq'/Fm was determined using a MINI-PAM II (Heinz Walz GmbH) to access the photophysiological perturbations due to stress exposure at the time-points represented by rectangular lines in Fig. 1b. Only one culture of the three technical replicates (pooled for transcriptome and metabolite analysis) per

timepoint and per biological replicate was measured to reduce the perturbations by the light pulse (intensity = 8 (pulse of 4000 µmol photons m^{-2} s^{-1}), frequency = 3, gain = 3) on metabolite and transcriptomic level.

Microscopy

Microscope pictures were taken in biological triplicates. For control, cold and heat stress conditions pictures were taken after 0 h and 24 h. For the HL/recovery time series after 6 h of stress and 4 h of recovery. The microscopical setup was comprised of a Carl Zeiss Axioscope 7 RL BF/DF/ C-DIC, TL LED with 10x, 20x, 40x and 100x objectives (Carl Zeiss Microscopy) connected to an Axiocam 208 color. The data was processed with the ZEN (blue edition; version 3.0) imaging system (Carl Zeiss Microscopy). For statistical analysis 6-10 (once 6 and once 8 for *Zygnema circumcarinatum*) pictures per replicate with 4-8 cells were evaluated (total of 40 cells).

Chemicals

Carotenoid standards of 9-*cis*-neoxanthin (≥ 97%), violaxanthin (≥ 90%), lutein (≥ 99%), α-carotene (≥ 95%), β-carotene (≥ 93%), and lycopene (≥ 90%) were obtained from Sigma Aldrich Chemie GmbH and Zeaxanthin (≥ 90%) from ChemPur GmbH. Chlorophyll a (≥ 95%) and b (≥ 95%) were obtained from Sigma Aldrich Chemie GmbH. Apocarotenoid standards of 6-methyl-5-hepten-2-one (≥ 99%), β-CC (≥ 97%) and β-IO (≥ 96%) were obtained from Sigma Aldrich Chemie GmbH. Dihydroactinidiolide (≥ 98%) was synthesized by abcr GmbH. β-IO-D_3 (≥ 95%) used as the internal standard for apocarotenoid quantification was obtained from Eptes. MTBE (≥99.5%) and methanol (≥99.8%) for HPLC analysis were obtained from Fisher Scientific GmbH and acetone for extraction and standard dilutions from Carl Roth GmbH (≥ 99.9%). Ethylacetate (≥ 99.9%) for apocarotenoid standard dilutions was obtained from Sigma Aldrich Chemie GmbH and methanol (≥ 99.9%) for standard dilutions from Fisher Scientific GmbH. Further solvents for carotenoid standard dilutions were dichloromethane (≥ 99.9%) from Carl Roth GmbH and acetonitrile (≥ 99.9%) from Fisher Scientific GmbH. BHT (≥ 99.7%) was obtained from Carl Roth GmbH. The water used for HPLC analysis and extraction was purified by ultrapure water system arium pro (Sartorius).

Carotenoid and chlorophyll extraction

Initially, the extraction protocol was inspired by Aronsson et al.[89] Several alterations were made to optimize the protocol for organisms investigated in this study, as follows. Prior to extraction, algae samples were lyophilized (ZIRBUS technology GmbH, Bad Grund, Germany) for 18–20 h and moss samples for circa 24 h. Samples were shielded from light during this process. Next, samples were immediately frozen again in liquid N_2 and homogenized quickly in reaction vials placed in a metal block (blockage of light and homogenous temperature) cooled by liquid N_2 (cooling and replacement of oxygen) with a sharp conical spatula to prevent oxidation or degradation. Samples were overlaid with argon again and stored at –80 °C until extraction. Directly before extraction samples were frozen in liquid N_2 again. All extractions were performed in a temperature-controlled room at 4 °C in the dark (only indirect light with an intensity below detection limit) to prevent alterations during extraction. Extraction solvents contained 0.1w% BHT to additionally prevent oxidation. Biomass was weighted quickly in the same room and the remaining sample was directly frozen again in liquid N_2 until HS-SPME-GC-MS analysis. 250–700 µL solvent A (acetone:water (80:20) + 0.1w% BHT) were added immediately to the weighted sample. Extraction volume was adjusted to the available/weighted biomass to ensure similar biomass:solvent ratios. This ratio was slightly optimized for each organism (average biomass used per mL of solvent-mix: *Mesotaenium endlicherianum* 5 mgDW/mL, *Zygnema circumcarinatum* 12 mgDW/mL, *Physcomitrium patens* 5 mgDW/mL) due to different pigment concentrations in different species. After adding solvent A the mixture was directly vortexed for circa 1-2 min (2-4 min for *Zygnema circumcarinatum* due to its worse extractability). Then, the sample was centrifuged for 1 min at 4 °C at max. speed 20238 rcf (Eppendorf 5424), and the supernatant was collected in another reaction tube. The procedure was repeated with solvent B (acetone + 0.1w% BHT) but the pellet was broken by stirring it up with a pipette tip before vortexing. The supernatants were combined, vortexed for 10 s and centrifuged again at max. speed to clear the extract from insolubles. 200 µL of the extract were transferred to a brown glass analysis vial with glass insert and PTFE

septum. Samples were injected (40 µL) into the HPLC within the next 5–25 min after extraction and stored on a cooled (10 °C) light shielded sample rack until analysis.

HPLC-UV-Vis analysis of carotenoids and chlorophylls

The HPLC system Agilent 1100 series equipped with a UV-Vis-DAD detector was used for simultaneous carotenoid and chlorophyl measurements. For separation a YMC Carotenoid C30 S- 3 µm column (250 x 4.6 mm I.D.) from YMC Europe was integrated. The solvent system used was initially inspired by Gupta et al.[90] but modified for this study, as follows. Eluents were degassed in an ultrasonic sonic bath (≥15 min) before connection with the HPLC system. A ternary gradient of eluent A (methanol:water, 98:2, v/v), eluent B (methanol:water, 95:2, v/v), and eluent C (MTBE) was applied as follows: 0 min A:C (80:20, flow rate 1.4 mL/min), 0–2.00 min gradient to A:C (70:30, flow rate 1.4 mL/min), 2.01 min B:C (70:30, flow rate 1.0 mL/min), 2.01–18.00 min gradient to B:C (0:100, flow rate 1.0 mL/min), 18:00–19.00 min gradient to A:C (80:20, flow rate 1.0 mL/min), 19.00–25.00 flow rate gradient from 1.0 mL/min to 1.4 mL/min A:C (80:20), hold for 1 min on this condition (total run time 26 min). The oven temperature was 20 °C.

Identities of the detected molecules were determined by absorption spectra, retention time, and comparison of both with authentical commercial standards (if available). In case of antheraxanthin[90] and respective *cis*/*trans*-isomers of carotenoids[90] identities of the detected molecules were determined by absorption spectra by comparison with literature data. Violaxanthin, lutein, α-carotene, β-carotene, and zeaxanthin were quantified at 451 nm based on calibration curves of the respective standards (Suppl. Figs. 2, 3, 4, and Suppl. Table 1). 9-*cis*-β-carotene was quantified based on β-carotene calibration due to similar spectral properties[91]. The analytical standard of 9-*cis*-neoxanthin was an almost equal mixture of isomers, so it was quantified based on violaxanthin calibration respecting differences in extinction coefficients instead[92] (Supplemental Table 2). Antheraxanthin (Supplemental Table 2) was quantified based on zeaxanthin calibration respecting differences in extinction coefficients[92]. Chlorophyll a and b were quantified at 660 nm based on calibration curves of the respective standards (Suppl. Figs. 2, 3, 4, and Suppl. Table 1).

HS-SPME-GC-MS analysis of volatile apocarotenoids

The method established here was initially based on Rivers et al.[93] The system used for volatile apocarotenoid measurements was comprised of the following technical compartments: GC/MSD instrument (Agilent Technologies 7890B) coupled to a 5977B MSD quadrupole, PAL3 Auto sampler system with Robotic Tool Change (RTC 120), polydimethylsiloxane/divinylbenzene/carboxen (50/30 µM DVB/CAR on PDMS) adsorbent SPME fiber from Supelco, HP-5MS UI column (30 m x 0,25 mm; 0,25 µm coating thickness; Agilent).

The temperature program for elution was the following: Inlet 250 °C, 60 °C 2 min hold, ramp 5 °C/min till 185 °C, ramp 25 °C/min till 320 °C followed by a 2 min hold, in total 34.4 min. Post run was set to 60 °C and Aux heater (MSD Transfer Line) to 280 °C. Helium gas flow rate was set to 1 mL/min.

Metabolite adsorption and desorption program: 30 min pre-conditioning at 270°C, 5 min sample equilibration at 70 °C with agitation, 40 min sample adsorption on fiber at 70 °C with agitation at a penetration depth of 40 mm followed by 35 min of sample desorption in the inlet at 250°C.

The electron impact ionisation energy (EI) was set to 70 eV and the ion source temperature was 230 °C.

Identities of the apocarotenoids were determined by fragmentation patterns and retention times by comparison with authentical analytical apocarotenoid standards in each species. For that purpose, total ion chromatograms (TIC) were recorded (m/z 40 – 300). All apocarotenoids were confirmed in all organisms by this measure except 6-methyl-5-hepten-2-one which was only detectable in selective ion monitoring (SIM) in *Zc* and *Pp*. For quantification SIM was used and recovery rates were accessed by co-injection and co-calibration (of each standard) with β-IO-D_3 (Suppl. Fig. 5); for respective chromatograms and fragmentation patterns, see Suppl. Figs. 6 to 12. Ions for quantification of the respective molecules: 6-methyl-5-hepten-2-one (m/Z: 108), β-cyclocitral (m/Z: 137) and β-IO (m/Z: 177), β-IO-D_3 (m/Z: 179 + 180), and dihydroactinidiolide (m/Z: 111).

The remaining refrozen samples used beforehand for carotenoid quantification (see above carotenoid and chlorophyll extraction) were weighted swiftly into brown glass HS-SPME-vials (20 mL, magnetic caps with silicone/PTFE septa) in a temperature-controlled room at 4 °C in the dark (only indirect light

with an intensity below detection limit) to prevent alterations by carotenoid degradation and co-injected with 4 µL β-IO-D_3 standard solution (same amount and concentration as for co-calibration). To reduce contamination by production residues and other volatiles in the HS-SPME-vials, they were precleaned as follows: Vials and caps were washed two times with methanol (≥ 99.9%) and dried overnight at 80 °C to emit remaining volatiles. After cooled down the vials were closed with the caps and stored until analysis.

RNA extraction

The RNA extraction was based on Dadras et al.[11] and slightly optimized for each organism. In general, the protocol described by the vendor of Spectrum Plant Total RNA Kit (Sigma) was used. Changes are described in the following. Frozen *Me* SAG 12.97 samples were put on ice, mixed immediately with 500 µL lysis buffer containing 2-mercaptoethanol (10 µL/mL lysis buffer), vortexed briefly and transferred for one minute to an ultrasonic bath for optimal cell penetration followed by 5 min of heat shock (56 °C). Protocol B (increased binding solution (750 µL)) was continued as described by vendor. For *Pp* extraction, the same protocol was used as for *Me* but with 1 mL lysis buffer and four minutes of ultrasonic bath. Frozen *Zc* SAG 698-1b samples were lyophilized freshly before extraction for 18-20 h (ZIRBUS technology GmbH, Bad Grund, Germany), frozen again in liquid N_2, put on ice, mixed immediately with 1 mL lysis buffer, vortexed briefly and transferred for four minutes to an ultrasonic bath for optimal cell penetration followed by 5 minutes of heat shock. Protocol B was continued as described by vendor.

Functional annotation

In order to assign functional information to the sequences we employed an comprehensive set of tools including InterProScan[94] (v5.64-96.0 and -pa -goterms flags), eggNOG-mapper[95-97] (v2.1.12 and -m diamond--dmnd_iterate yes--dbmem --cpu 0 --evalue 1e-10 --sensmode ultra-sensitive --tax_scope 33090 --dmnd_db eggnog_proteins_default_viridiplantae.dmnd flags), BLAST[98] (v2.15.0) against protein files of *A. thaliana*[99] and genome scale gene family analysis using Orthofinder[100-103] (v2.5.5). *Me*, *Zc* SAG698-1b and *Pp* had 74.5, 93.9, and 78.1% of their genes in HOGs and they have 8.2, 2.2, 12% or their genes in species-specific orthogroups, respectively. We first ran Orthofinder with these settings: -S diamond -M msa -A mafft -T fasttree -t 200 -a 6 -y. Building on this, we redid the analysis by providing a user-defined rooted species tree to increase the accuracy of the inference and this tree includes the following species: *Anthoceros agrestis* oxford[104], *Azolla filiculoides*[105], *A. thaliana* [99], *Brachypodium distachyon* [106], *Chara braunii*[6], *Chlorokybus melkonianii*[9,107], *Chlamydomonas reinhardtii* [108], *Closterium sp.* NIES-67[109], *Klebsormidium nitens*[5], *Mesotaenium endlicherianum*[7,11], *Marchantia polymorpha* [110], *Mesostigma viride* [111], *Ostreococcus lucimarinus* [112], *Oryza sativa* [113], *Prasinoderma coloniale* [114], *Penium margaritaceum* [115], *Physcomitrium patens*[39], *Solanum lycopersicum* [116], *Selaginella moellendorffii* [117], *Spirogloea muscicola*[7], *Zygnema circumcarinatum*[10] SAG 698-1a, *Z. circumcarinatum*[10] SAG 698-1b, *Z. circumcarinatum*[10] UTEX 1559, *Z. circumcarinatum*[10] UTEX 1560, and *Zea mays*[118]. To assign GO terms to each gene, we combined the functional annotation of InterProScan and eggNOG-mapper into a table for each species using the ontologyIndex package (v2.11) [119]. We also used Tapscan (v2)[120] to identify transcription factors for each species.

Quality control and gene expression quantification and exploratory data analysis

We used the pipeline of Dadras et al.[11] built using Snakemake (v7.7.0) [121] and available on GitHub (https://github.com/dadrasarmin/rnaseq_quantification_kallisto_pipeline). Briefly, we used FastQC (v0.12.1)[122] and MultiQC (v1.16)[123] to perform quality control, Trimmomatic (v0.39)[124] to perform trimming and filtering, and Kallisto (v0.48.0)[125] to quantify gene expressions.

We used R (v4.3.2)[126] and tidyverse (v2.0.0)[127] for data analysis and visualization. We used tximport (v1.30.0)[128] to import and summarize count tables at gene-level into R and normalized count tables for both sequencing depth and gene length using the following settings: “countsFromAbundance = "lengthScaledTPM", txOut = F”. We used edgeR (v4.0.6)[129] to keep only genes with expression levels higher than 10 counts-per-milion (CPM) in at least 3 samples. Based on the experimental design of this study, we chose to perform global normalization (quantile normalization) to remove technical unwanted variations in our dataset[130]. We used qsmooth (v1.18.0)[131] with treatments as group_factor to perform the normalization.

Differential gene expression analysis

We used limma (v3.58.1)[132] to model gene expression changes under each treatment samples compared to the same time point in the control condition using lmFit, contrasts.fit, eBayes, decideTests functions. We picked |log2(fold change)| >= 1 as well as Benjamini-Hochberg method for p-value adjustment and a threshold of 0.05 to determine differentially expressed genes (DEGs). We used GO-gene tables that we prepared in the functional annotation step to perform Over-Representation Analysis (ORA) using clusterProfiler (v4.10.0)[133]. In this section, we only focused on "Biological Process" domain of GO terms, using only expressed genes in our dataset as background, adjusted p. value cut off <= 0.05 and q. value cut off <= 0.05 for enrichment analysis. To visualize the general pattern of GO term enrichment over-time under each treatment, we used alluvial (v0.2.0)[134] and picked top 10 GO terms that are enriched in as many as possible time points and sorted them on Y-axis based on the enriched gene count of the GO term. The thickness of each stratum is visualized based on the number of enriched genes in each GO term.

Co-expression network analysis

It is well known that gene co-expression methods, each with its own strengths and weaknesses, can lead the different final networks[135]. In this study, we used two methods from different classes of co-expression network analysis. First, we use Weighted Gene Co-expression Network Analysis (WGCNA v1.72.5)[136] to infer one network from all treatments and time points per species. In this method, correlation measures are used to calculate an adjacency matrix using a beta and a network type. Next, the topological overlap matrix is calculated based on the adjacency matrix, then a distance matrix will be calculated and using hierarchical clustering genes will be divided into various modules. Finally, modules that are very similar based on their Eigenvalues will be merged. We followed the authors' recommendations for the parameters for this last step. In summary, we screened soft-thresholding powers from 1 to 50 for each species and picked a soft threshold based on mean connectivity (around 50), median connectivity (around 20), and signed R^2 of Scale free topology model fit (above 0.8). We picked 20, 20, 14 as soft threshold for *Me*, *Pp*, and *Zc*. We built our networks using the following settings: Merging threshold=0.20, correlation method= biweight midcorrelation, network type=signed, TOMType=signed, minimum module size=30, and maximum percentile of outliers=0.05. We calculated Pearson's correlation coefficient and gene significance based on module's Eigengene values and various physiological measurements and metabolite concentration changes. We also calculated inter- and intra-modular connectivity for each module and picked top 20 highly connected genes as the hubs of that module. For each module, we performed GO enrichment analysis similar to the differential gene expression analysis mentioned above. Biological theme comparison plots were made using clusterProfiler to discover patterns of GO enrichment among different modules. We used igraph (v1.6.0)[137] to visualize co-expression network for each module and annotate the hubs. We annotated hubs based on the blast results described in the functional annotation above in this order: (a) gene symbol > (b) *A. thaliana* best hit gene ID > (c) species gene ID.

The second method is the Dirichlet Process Gaussian Process mixture model (DPGP), a non-parametric model-based method that is designed to perform gene co-expression analysis for time series datasets. It solves the problem of the number of clusters using a Dirichlet process and then model the dependencies in gene expression profiles between time points using a Gaussian model[44]. We used fold change values that has a significant adjusted p-value ≤ 0.05 compared to the same time point in control as the input of the software. Due to assumptions of this method, we had to make one network per species (*Me*, *Zc*, *Pp*) and per treatment (cold, heat, HL); nine networks in total. We visualized expression profiles and performed GO enrichment analysis as mentioned above. The authors of DPGP suggested that this tool can be used to look for tightly regulated genes by filtering for gene assignments to clusters with a specific threshold in the final probability. We picked probability $\geq$ 0.7 as our threshold as suggest by the DPGP authors and compared inter- and intra-species similarities between clusters using Jaccard distance.

We picked a collection of the most similar filtered gene clusters based on Jaccard distances to investigate further. We normalized the data between 0 to 1 to visualize it as a heatmap. Also, we put a minimum cap of 0.9 Jaccard distance for both clustering methods since the heatmap was not informative due to presence of few outliers in pair-wise combinations (very close clusters).

Gene regulatory network (GRN) inference

There are various methods to calculate GRN based on time series transcriptomics but the balance between run time and accuracy makes it hard to pick a gold standard among all methods. Here, we used Sliding Window Inference for Network Generation (SWING)[45] to account for our temporal information which is one of the best method for this purpose according to independent benchmarkings[138]. SWING uses a multivariate Granger causality to infer network topology from time series data. We combined the transcriptomics data with metabolite concentrations as inputs and used the Random Forest (RF, i.e. SWING-RF) method to infer the network which has the best performance compared to LASSO and PLSR in the benchmarking[138]. The parameters that should be defined to infer the network were decided based on the best practice that was suggested by the authors of SWING as follows; For Me, we had more metabolite data and we picked: minimum lag= 0, maximum lag = 1, fixed-length of sliding window = 4 and number of trees = 500. For Pp and Zc, we picked these parameters: minimum lag = 0, maximum lag = 1, fixed-length of sliding window = 2 and number of tress = 500. We performed Z-score transformation on the input datasets. To integrate scores from many windows and delays into a single score (regulator-regulated pairs), we utilized this package's mean-mean aggregation approach. Confidence values from windowed subsets are combined into a single network by calculating the mean rank of the edge at each delay k, followed by the average rank of the edge over all delays.

The outcome of this method is a ranked list of all possible pairs ordered from the most to the less confident one. We first filtered out pairs with 0 support, extracted the top 0.1%, and visualized the result via igraph. Since it was still a very big network, then investigated the network with more filtering. Basically we created file list based on keywords downloaded from TAIR. (a) Cold consists of "cold acclimation", "response to cold", and "cellular response to cold" (b) Heat consists of "response to heat", "heat acclimation", "cellular response to heat", and "cellular heat acclimation" (c) HL consists of "response to high light intensity", and "cellular response to high light intensity" (d) Oxidative consists of "response to oxidative stress", "cellular response to oxidative stress", "cellular response to reactive oxygen species", "response to photooxidative stress", and "regulation of response to oxidative stress" (e) "Carotenoid metabolic process" (f) "Apocarotenoid metabolic process". We then used the BLAST results mentioned above to find possible homologs of these genes in our species of interest. We used these gene sets as well as metabolite list and TF list extracted using TapScan to look for top 0.1% edges of GRN for each of these subsets. We used igraph to visualize the data and annotate the top 100 nodes in the edge list as explained in the co-expression network section.

Data availability

All RNAseq reads have been uploaded to NCBI SRA and can be accessed under Bioproject PRJNA895341 (*Mesotaenium*) and PRJNA939006 (*Zygnema* and *Physcomitrium*) and SRA accessions from SRR22077315 to SRR22077409 (*Mesotaenium*) and from SRR23625966 to SRR23626145 (*Zygnema* and *Physcomitrium*).

Code is available here: https://gitlab.gwdg.de/armin.dadras/time-resolved-oxidative-signal-convergence-across-the-algae-embryophyte-divide

Raw metabolite profiling data are available on Zenodo: 10.5281/zenodo.10805605

Data can be interactively explored at https://rshiny.gwdg.de

ACKNOWLEDGEMENTS

We thank René Heise, Sabine Freitag, Malte Bürsing, and Tarek Morsi for excellent technical support and Greta Lisbach for help during experimentation. J.d.V. thanks the European Research Council for funding under the European Union's Horizon 2020 research and innovation programme (Grant Agreement No. 852725; ERC-StG "TerreStriAL"). J.d.V. and I.F. are grateful for support through the German Research Foundation (DFG): on the grant SHOAL (514060973; VR132/11-1) and within the framework of the Priority Programme "MAdLand – Molecular Adaptation to Land: Plant Evolution to Change" (SPP 2237; 440231723 VR 132/4-1; VR 132/4-2; FE 446/14-1), in which T.R. is a PhD student and A.D., J.M.R.F.-J, and I.I. partake as associate members. A.D. is grateful for being supported through the International Max Planck Research School (IMPRS) for Genome Science. J.M.R.F.-J. and

T.R. gratefully acknowledge support by the Ph.D. program "Microbiology and Biochemistry" within the framework of the “Göttingen Graduate Center for Neurosciences, Biophysics, and Molecular Biosciences” (GGNB) at the University of Goettingen.

CONTRIBUTIONS

J.d.V. conceived the project. J.d.V. coordinated the project with I.F., J.d.V. and T.P.R. designed the experiments. T.P.R., T.D., S.P., N.H., C.H., S.d.V., I.I., and T.P. performed experimental work. A.D. and J.d.V. designed the computational analysis. A.D. carried out computational analysis. T.P.R. and C.H. performed analytics. C.H. and I.F. supervised the analytics. R.P. and S.A.R. predicted streptophyte transcription factors. J.d.V., A.D., and T.P.R. contributed to writing the manuscript. J.d.V. organized and wrote the final manuscript. All authors commented, discussed, and provided input on the final manuscript.

COMPETING INTERESTS

The authors declare no competing interests.

EXTENDED DATA FIGURE

Extended Data Figure 1: Differential gene expression comparisons highlight heat responsiveness. Significance of gene expression change as $\log_2$(fold change) due to stress exposure in all three species. (a) Pie diagrams of the respective portion of 2-fold up to ≥4-fold up and downregulated genes and corresponding Volcano plots with adjusted *P*-value ($\log_{10}$-scaled). (b) Bar plots of $\log_{10}$ adjusted counts of the number of significantly 2-fold and ≥4-fold up and downregulated genes.

Extended Data Figure 2: Alluvial plots on GO terms associated with high light recovery. Time-resolved alluvial diagrams of most prominent GO terms principally conserved in all three species with all associated differentially regulated genes (number indicated by line width) during high light recovery under control conditions, category time scale. Note the delayed responses in *Zygnema circumcarinatum.*

Extended Data Figure 3: Biological theme comparison of GO terms pinpointed by significantly regulated genes. Most enriched GO terms among the significantly differentially expressed genes in 51 comparisons (stress versus control) represented by color code in all three organisms and their relative enrichment shown by pie slice size and number of genes per GO term represented by circle size of pie plots.

Extended Data Figure 4: Biological theme comparison of GO terms associated with modules recovered by WGCNA. Color coded comparison of clusters of most enriched GO terms in respective WGCNA clusters in a *Zygnema circumcarinatum, Physcomitrium patens,* and *Mesotaenium endlicherianum.* Number of genes per enriched GO term is represented by the size of the circles.

Extended Data Figure 5: GO terms and hubs in modules recovered by WGCNA. (a,b,c,e,g,h,i) Most enriched genes and GO terms in some representative WGCNA clusters from Figure 2. (d) dotplot of enriched GO terms. (f,j) Cnet plot of enriched GO terms.

Extended Data Figure 6: GO terms enriched in DPGP. Significantly enriched GO terms of some DPGP clusters of Figure 5 including all three species.

Extended Data Figure 7: All shared connections predicted across all networks inferred via SWING. SWING-RF network filtered based on HOGs and metabolites conserved in all

three species. Hierarchical orthogroups (HOGs) are annotated if they engage in the top 100 most predictive relationships. Two networks (a and b) were recovered.

Extended Data Figure 8: Predicted gene regulatory network, via SWING, annotated based on best BLAST hits (BBH). SWING-RF of 100 most predictive (enlarged circles) genes (best BLAST hit-defined homologs) and metabolites conserved in all three species. Two networks (a and b) were recovered: (a) an 'AHK centered' cluster; (b) Central stress responsive cluster resembling some important parts of Figure 6. Homologs are annotated if they engage in the top 100 most predictive relationships.

Extended Data Figure 9: Predicted gene regulatory network, via SWING, computed with all time points for which transcriptome data were generated. A predicted gene regulatory network of 900 nodes and edges. HOGs are annotated if they engage in the top 100 most predictive relationships across all three species. Yellow nodes are genes that have been recovered in both the SWING networks (i.e. with all time points and only those time points for which also metabolite data were generated, see Figure 6 and Extended Data Figures 7 and 8). Orange nodes are genes that, upon recomputing the network with all time series data, became some of the 100 most predictive. Purple indicates genes that were among the top 100 most predictive genes in the networks that included the metabolite data but are now among the ranks 800 to 900. Grey nodes are genes that were in both predictions not in the top 100.

FIGURE LEGENDS

Figure 1: A time-series setup for stress kinetics in three 600-million-year-divergent streptophytes. (a) Cladogram of Streptophyta; Phragmoplastophyta studied herein are highlighted in bold. (b) Summary of the stress experiment time grids and the respective investigations including RNAseq, metabolite profiling, photophysiology, and morphology. *Me* specific metabolite profiling is indicated by black dots. For high light stress experiments morphology was investigated at maximum stress (yellow dot) and maximum recovery. (c) Boxplots of relative quantum yield of PSII (Fq'/Fm') during stress exposure and control, category time scale. (d) Boxplots of aggregated relative quantum yield of PSII (Fq'/Fm') due to stress exposure and in control. (e) Scatterplots with Loess fit of relative quantum yield of PSII (Fq'/Fm') during stress exposure and control of first six hours of the experiment, absolute time scale. (f) Morphological observations before and after stress exposure with time points corresponding to b. (g) Quantification of observed morphological effects; statistics was performed using a Kruskal-Wallis plus Dunn post-hoc test. LDs = accumulated lipid droplets/small droplets, red/brown = overall color change of cell to a more red-brown shade, DPN = droplets accumulated around the nucleus.

Figure 2: Divergent temporal stress progression retraced by global differential gene expression analysis. (a) PCA analyses for all three species with color and symbol code for the respective RNAseq samples on the right; below the PCAs, time-dependent changes in the data are highlighted in plots of time versus PC1 and PC2. (b) Time-resolved alluvial diagrams of most prominent GO terms found across at least three time points based on significantly differentially regulated genes (term size indicated by line width) during cold, heat and high light stress exposure, category time scale.

Figure 3: Carotenoid and apocarotenoid dynamics upon stress. (a) Simplified schematic representation of the conserved and intertwined carotenoid and apocarotenoid pathways in the three organisms of this work. (b) Heatmap of metabolite flux and its correlation with the

different conditions/samples; the color and symbol codes are as in Figure 2 and can be found in the bottom right corner of the figure. (c) Pigment pool fluctuations due to stress exposure. Areas relative to size of pigment pool/contribution of individual pigment to the pool normalized on *Pp* t_0. (d) Expression changes of important genes in the first 6 h of stress exposure (only one respective homolog shown also in some cases more were present). (e) Relative change of selected metabolite levels/ratios in the first 6 h of stress exposure relative to the average value of t_0 normalized by DW of sample, recovery rate of measurement, and molecular mass of the respective metabolites. 6MHO, 6-methyl-5-hepten-2-one, 9-cis, 9-*cis*-β-Carotene, 9-*cis*-neo, 9-*cis*-Neoxanthin, (A+Z)/(V+A+Z), (Antheraxanthin+Zeaxanthin) / (Violaxanthin+Antheraxanthin+Zeaxanthin), α-car, α-Carotene, antherax, Antheraxanthin, β-car, β-Carotene, β-car/9-*cis*-neox, β-Carotene / 9-*cis*- β-Carotene, β-Car/ β-CC, β-Carotene / β-Cyclocitral, β-Car/ β-IO, β-Carotene / β-Ionone, β-Car/DHA, beta β-Carotene / Dihydroactinidiolide, β-Car/ β-CC+β-IO+DHA, β-Carotene / (β-Cyclocitral + β-Ionone + Dihydroactinidiolide), β-CC, β-Cyclocitral, β-IO, β-Ionone, Chl *a*, Chlorophyll *a*, Chl *a* / *b*, Chlorophyll *a* / Chlorophyll *b*, Chl *b*, Chlorophyll *b*, DHA, Dihydroactinidiolide, DHA/β-IO, Dihydroactinidiolide / β-Ionone, violax, Violaxanthin, V+A+Z/Chl*a*+Chl*b*, (Violaxanthin+Antheraxanthin+Zeaxanthin) / (Chlorophyll *b*), Zeax, Zeaxanthin.

Figure 4: Unsupervised gene co-expression networks recover shared programs. WGCNA was used to compute co-expression networks. (a) Distance dendograms of module correlation with metabolites, condition, and photophysiology. (b) Heatmaps of module trait correlation with metabolites, condition, and photophysiology corresponding to distance trees in a. (c) Scaled Jaccard distances that illustrate similarity (pink) and dissimilarity (blue) between modules based on HOGs. (d) The 50 most similar modules. (e) cnetplot of the GO terms enriched in the cluster *Me*brown (f-j) Selected WGCNA clusters with the top 20 most connected genes annotated based on homology. (k) WGCNA cluster correlation of assigned most enriched GO terms in *Zygnema circumcarinatum*, *Physcomitrium patens* and *Mesotaenium endlicherianum*.

Figure 5: Time-course gene expression clusters pinpoint shared responders. Dirichlet Process Gaussian Process (DPGP) time-resolved clusters of stress samples. (a) Top: Heatmap of Jaccard distances computed for all DPGP clusters based on HOGs; bottom: zoom-in on the top 50 most similar cluster (b) Line plots of the expression behavior of cohorts of genes recovered by DPGP clustering for 20 pairs of DPGP clusters high Jaccard similarity; the Z-score standardized $\log_2$ fold change (CPM) over the first 6 hours of stress exposure is shown. (c) Left: Black ticks indicate into which DPGP clusters the hub genes recovered by WGCNA (indicated by colors) fall; right: line plots of the expression behavior of cohorts of genes in DPGP clusters that are particularly rich in WGCNA-defined hub genes.

Figure 6: A predicted gene regulatory network shared across 600 million years of streptophyte evolution. SWING-RF network filtered based on conserved DPGP clusters of most predictive (enlarged circles) HOGs and metabolites conserved in all three species. (a) Predicted conserved stress responsive network with some important hubs highlighted. (b) Zoom into the central 'kinome' (LRR) SPS kinases hub. (c) Ranked position of top 50 most connected nodes in the conserved network among all networks predicted by SWING (not filtered). (d) Ranked position of top 50 most connected nodes in the conserved network among all networks predicted by SWING and filtered for genes in conserved DPGP clusters.

REFERENCES

1 Bar-On, Y. M., Phillips, R. & Milo, R. The biomass distribution on Earth. *Proc Natl Acad Sci U S A* **115**, 6506-6511 (2018). https://doi.org:10.1073/pnas.1711842115

2 Initiative, O. T. P. T. One thousand plant transcriptomes and the phylogenomics of green plants. *Nature* **574**, 679-685 (2019).

3 Wickett, N. J. *et al.* Phylotranscriptomic analysis of the origin and early diversification of land plants. *Proceedings of the National Academy of Sciences* **111**, E4859-E4868 (2014).

4 Puttick, M. N. *et al.* The interrelationships of land plants and the nature of the ancestral embryophyte. *Current Biology* **28**, 733-745. e732 (2018).

5 Hori, K. *et al.* Klebsormidium flaccidum genome reveals primary factors for plant terrestrial adaptation. *Nature communications* **5**, 3978 (2014).

6 Nishiyama, T. *et al.* The Chara genome: secondary complexity and implications for plant terrestrialization. *Cell* **174**, 448-464. e424 (2018).

7 Cheng, S. *et al.* Genomes of subaerial Zygnematophyceae provide insights into land plant evolution. *Cell* **179**, 1057-1067. e1014 (2019).

8 Jiao, C. *et al.* The Penium margaritaceum genome: hallmarks of the origins of land plants. *Cell* **181**, 1097-1111. e1012 (2020).

9 Wang, S. *et al.* Genomes of early-diverging streptophyte algae shed light on plant terrestrialization. *Nature Plants* **6**, 95-106 (2020).

10 Feng, X. *et al.* Chromosome-level genomes of multicellular algal sisters to land plants illuminate signaling network evolution. *bioRxiv* (2023). https://doi.org:10.1101/2023.01.31.526407

11 Dadras, A. *et al.* Environmental gradients reveal stress hubs pre-dating plant terrestrialization. *Nature Plants* (2023). https://doi.org:10.1038/s41477-023-01491-0

12 Donoghue, P. C. J., Harrison, C. J., Paps, J. & Schneider, H. The evolutionary emergence of land plants. *Curr Biol* **31**, R1281-R1298 (2021). https://doi.org:10.1016/j.cub.2021.07.038

13 Mulvey, H. & Dolan, L. RHO of plant signaling was established early in streptophyte evolution. *Curr Biol* (2023). https://doi.org:10.1016/j.cub.2023.11.007

14 Bierenbroodspot, M. J. *et al.* Phylogenomic insights into the first multicellular streptophyte. *Current Biology* **34** (2024). https://doi.org:10.1016/j.cub.2023.12.070

15 Bowman, J. L., Sakakibara, K., Furumizu, C. & Dierschke, T. Evolution in the Cycles of Life. *Annu Rev Genet* **50**, 133-154 (2016). https://doi.org:10.1146/annurev-genet-120215-035227

16 Delaux, P. M. *et al.* Algal ancestor of land plants was preadapted for symbiosis. *Proc Natl Acad Sci U S A* **112**, 13390-13395 (2015). https://doi.org:10.1073/pnas.1515426112

17 Delaux, P. M. & Schornack, S. Plant evolution driven by interactions with symbiotic and pathogenic microbes. *Science* **371** (2021). https://doi.org:10.1126/science.aba6605

18 Fürst-Jansen, J. M., de Vries, S. & de Vries, J. Evo-physio: on stress responses and the earliest land plants. *Journal of Experimental Botany* **71**, 3254-3269 (2020).

19 Scheres, B. & van der Putten, W. H. The plant perceptron connects environment to development. *Nature* **543**, 337-345 (2017). https://doi.org:10.1038/nature22010

20 Glasser, C. *et al.* Meta-analysis of retrograde signaling in Arabidopsis thaliana reveals a core module of genes embedded in complex cellular signaling networks. *Mol Plant* **7**, 1167-1190 (2014). https://doi.org:10.1093/mp/ssu042

21 Pfannschmidt, T. Chloroplast redox signals: how photosynthesis controls its own genes. *Trends Plant Sci* **8**, 33-41 (2003). https://doi.org:10.1016/s1360-1385(02)00005-5

22 Kleine, T. *et al.* Acclimation in plants - the Green Hub consortium. *Plant J* **106**, 23-40 (2021). https://doi.org:10.1111/tpj.15144

23 Nisar, N., Li, L., Lu, S., Khin, N. C. & Pogson, B. J. Carotenoid metabolism in plants. *Mol Plant* **8**, 68-82 (2015). https://doi.org:10.1016/j.molp.2014.12.007

24 Sandmann, G. Diversity and origin of carotenoid biosynthesis: its history of coevolution towards plant photosynthesis. *New Phytol* **232**, 479-493 (2021). https://doi.org:10.1111/nph.17655

25 Hou, X., Rivers, J., Leon, P., McQuinn, R. P. & Pogson, B. J. Synthesis and Function of Apocarotenoid Signals in Plants. *Trends Plant Sci* **21**, 792-803 (2016). https://doi.org:10.1016/j.tplants.2016.06.001

26 Moreno, J. C., Mi, J., Alagoz, Y. & Al-Babili, S. Plant apocarotenoids: from retrograde signaling to interspecific communication. *Plant J* **105**, 351-375 (2021). https://doi.org:10.1111/tpj.15102

27 Ramel, F. *et al.* Carotenoid oxidation products are stress signals that mediate gene responses to singlet oxygen in plants. *Proc Natl Acad Sci U S A* **109**, 5535-5540 (2012). https://doi.org:10.1073/pnas.1115982109

28 D'Alessandro, S., Mizokami, Y., Legeret, B. & Havaux, M. The Apocarotenoid beta-Cyclocitric Acid Elicits Drought Tolerance in Plants. *iScience* **19**, 461-473 (2019). https://doi.org:10.1016/j.isci.2019.08.003

29 Lundquist, P. K. *et al.* Loss of plastoglobule kinases ABC1K1 and ABC1K3 causes conditional degreening, modified prenyl-lipids, and recruitment of the jasmonic acid pathway. *Plant Cell* **25**, 1818-1839 (2013). https://doi.org:10.1105/tpc.113.111120

30 Mitra, S. *et al.* Negative regulation of plastidial isoprenoid pathway by herbivore-induced beta-cyclocitral in Arabidopsis thaliana. *Proc Natl Acad Sci U S A* **118** (2021). https://doi.org:10.1073/pnas.2008747118

31 Felemban, A. *et al.* The apocarotenoid beta-ionone regulates the transcriptome of Arabidopsis thaliana and increases its resistance against Botrytis cinerea. *Plant J* (2023). https://doi.org:10.1111/tpj.16510

32 Nambara, E. & Marion-Poll, A. Abscisic acid biosynthesis and catabolism. *Annu Rev Plant Biol* **56**, 165-185 (2005). https://doi.org:10.1146/annurev.arplant.56.032604.144046

33 Cutler, S. R., Rodriguez, P. L., Finkelstein, R. R. & Abrams, S. R. Abscisic acid: emergence of a core signaling network. *Annu Rev Plant Biol* **61**, 651-679 (2010). https://doi.org:10.1146/annurev-arplant-042809-112122

34 Barbier, F., Fichtner, F. & Beveridge, C. The strigolactone pathway plays a crucial role in integrating metabolic and nutritional signals in plants. *Nat Plants* **9**, 1191-1200 (2023). https://doi.org:10.1038/s41477-023-01453-6

35 Kleine, T. & Leister, D. Retrograde signaling: Organelles go networking. *Biochim Biophys Acta* **1857**, 1313-1325 (2016). https://doi.org:10.1016/j.bbabio.2016.03.017

36 Havaux, M. beta-Cyclocitral and derivatives: Emerging molecular signals serving multiple biological functions. *Plant Physiol Biochem* **155**, 35-41 (2020). https://doi.org:10.1016/j.plaphy.2020.07.032

37 D'Alessandro, S. & Havaux, M. Sensing beta-carotene oxidation in photosystem II to master plant stress tolerance. *New Phytol* **223**, 1776-1783 (2019). https://doi.org:10.1111/nph.15924

38 Lenton, T. M. *et al.* Earliest land plants created modern levels of atmospheric oxygen. *Proc Natl Acad Sci U S A* **113**, 9704-9709 (2016). https://doi.org:10.1073/pnas.1604787113

39 Lang, D. *et al.* The Physcomitrella patens chromosome-scale assembly reveals moss genome structure and evolution. *Plant J* **93**, 515-533 (2018). https://doi.org:10.1111/tpj.13801

40 Hess, S. *et al.* A phylogenomically informed five-order system for the closest relatives of land plants. *Current Biology* **32**, 4473-4482. e4477 (2022).

41 de Vries, J. *et al.* Heat stress response in the closest algal relatives of land plants reveals conserved stress signaling circuits. *The Plant Journal* **103**, 1025-1048 (2020).

42 Shumbe, L., Bott, R. & Havaux, M. Dihydroactinidiolide, a high light-induced beta-carotene derivative that can regulate gene expression and photoacclimation in Arabidopsis. *Mol Plant* **7**, 1248-1251 (2014). https://doi.org:10.1093/mp/ssu028

43 Hare, P. D., Moller, S. G., Huang, L. F. & Chua, N. H. LAF3, a novel factor required for normal phytochrome A signaling. *Plant Physiol* **133**, 1592-1604 (2003). https://doi.org:10.1104/pp.103.028480

44 McDowell, I. C. *et al.* Clustering gene expression time series data using an infinite Gaussian process mixture model. *PLoS computational biology* **14**, e1005896 (2018).

45 Finkle, J. D., Wu, J. J. & Bagheri, N. Windowed Granger causal inference strategy improves discovery of gene regulatory networks. *Proc Natl Acad Sci U S A* **115**, 2252-2257 (2018). https://doi.org:10.1073/pnas.1710936115

46 Yuan, F. *et al.* OSCA1 mediates osmotic-stress-evoked Ca2+ increases vital for osmosensing in Arabidopsis. *Nature* **514**, 367-371 (2014). https://doi.org:10.1038/nature13593

47 Takahashi, S., Ogawa, T., Inoue, K. & Masuda, T. Characterization of cytosolic tetrapyrrole-binding proteins in Arabidopsis thaliana. *Photochem Photobiol Sci* **7**, 1216-1224 (2008). https://doi.org:10.1039/b802588f

48 Lee, H. J., Mochizuki, N., Masuda, T. & Buckhout, T. J. Disrupting the bimolecular binding of the haem-binding protein 5 (AtHBP5) to haem oxygenase 1 (HY1) leads to oxidative stress in Arabidopsis. *J Exp Bot* **63**, 5967-5978 (2012). https://doi.org:10.1093/jxb/ers242

49 Xing, Q. *et al.* ZHOUPI controls embryonic cuticle formation via a signalling pathway involving the subtilisin protease ABNORMAL LEAF-SHAPE1 and the receptor kinases GASSHO1 and GASSHO2. *Development* **140**, 770-779 (2013). https://doi.org:10.1242/dev.088898

50 Tanaka, H. *et al.* A subtilisin-like serine protease is required for epidermal surface formation in Arabidopsis embryos and juvenile plants. *Development* **128**, 4681-4689 (2001). https://doi.org:10.1242/dev.128.23.4681

51 Murase, K., Hirano, Y., Sun, T. P. & Hakoshima, T. Gibberellin-induced DELLA recognition by the gibberellin receptor GID1. *Nature* **456**, 459-463 (2008). https://doi.org:10.1038/nature07519

52 Jeon, J. *et al.* A subset of cytokinin two-component signaling system plays a role in cold temperature stress response in Arabidopsis. *J Biol Chem* **285**, 23371-23386 (2010). https://doi.org:10.1074/jbc.M109.096644

53 Tran, L. S. *et al.* Functional analysis of AHK1/ATHK1 and cytokinin receptor histidine kinases in response to abscisic acid, drought, and salt stress in Arabidopsis. *Proc Natl Acad Sci U S A* **104**, 20623-20628 (2007). https://doi.org:10.1073/pnas.0706547105

54 Bowman, J. L., Briginshaw, L. N., Fisher, T. J. & Flores-Sandoval, E. Something ancient and something neofunctionalized—evolution of land plant hormone signaling pathways. *Current Opinion in Plant Biology* **47**, 64-72 (2019).

55 Van de Poel, B. & de Vries, J. Evolution of ethylene as an abiotic stress hormone in streptophytes. *Environ Exp Bot* **214**, 105456 (2023). https://doi.org:10.1016/j.envexpbot.2023.105456

56 Van de Poel, B., Cooper, E. D., Van Der Straeten, D., Chang, C. & Delwiche, C. F. Transcriptome profiling of the green alga Spirogyra pratensis (Charophyta) suggests an ancestral role for ethylene in cell wall metabolism, photosynthesis, and abiotic stress responses. *Plant Physiology* **172**, 533-545 (2016).

57 Ju, C. *et al.* Conservation of ethylene as a plant hormone over 450 million years of evolution. *Nature plants* **1**, 14004 (2015).

58 Yasumura, Y., Pierik, R., Fricker, M. D., Voesenek, L. A. & Harberd, N. P. Studies of Physcomitrella patens reveal that ethylene-mediated submergence responses arose relatively early in land-plant evolution. *Plant J* **72**, 947-959 (2012). https://doi.org:10.1111/tpj.12005

59 O'Malley, R. C. *et al.* Ethylene-binding activity, gene expression levels, and receptor system output for ethylene receptor family members from Arabidopsis and tomato. *Plant J* **41**, 651-659 (2005). https://doi.org:10.1111/j.1365-313X.2004.02331.x

60 Yu, K. *et al.* The Kelch-F-box protein SMALL AND GLOSSY LEAVES 1 (SAGL1) negatively influences salicylic acid biosynthesis in Arabidopsis thaliana by promoting the turn-over of transcription factor SYSTEMIC ACQUIRED RESISTANCE DEFICIENT 1 (SARD1). *New Phytol* **235**, 885-897 (2022). https://doi.org:10.1111/nph.18197

61 Yu, S. I., Kim, H., Yun, D. J., Suh, M. C. & Lee, B. H. Post-translational and transcriptional regulation of phenylpropanoid biosynthesis pathway by Kelch repeat F-box protein SAGL1. *Plant Mol Biol* **99**, 135-148 (2019). https://doi.org:10.1007/s11103-018-0808-8

62 Harmon, F. G. & Kay, S. A. The F box protein AFR is a positive regulator of phytochrome A-mediated light signaling. *Curr Biol* **13**, 2091-2096 (2003). https://doi.org:10.1016/j.cub.2003.11.019

63 Shumbe, L. *et al.* METHYLENE BLUE SENSITIVITY 1 (MBS1) is required for acclimation of Arabidopsis to singlet oxygen and acts downstream of beta-cyclocitral. *Plant Cell Environ* **40**, 216-226 (2017). https://doi.org:10.1111/pce.12856

64 Atanasov, V. *et al.* Arabidopsis BBX14 is involved in high light acclimation and seedling development. *Plant J* (2023). https://doi.org:10.1111/tpj.16597

65 Zhang, Z. *et al.* CONSTANS-LIKE 7 (COL7) is involved in phytochrome B (phyB)-mediated light-quality regulation of auxin homeostasis. *Mol Plant* **7**, 1429-1440 (2014). https://doi.org:10.1093/mp/ssu058

66 Liu, L. J. *et al.* COP1-mediated ubiquitination of CONSTANS is implicated in cryptochrome regulation of flowering in Arabidopsis. *Plant Cell* **20**, 292-306 (2008). https://doi.org:10.1105/tpc.107.057281

67 Muller, M. & Munne-Bosch, S. Ethylene Response Factors: A Key Regulatory Hub in Hormone and Stress Signaling. *Plant Physiol* **169**, 32-41 (2015). https://doi.org:10.1104/pp.15.00677

68 Toriyama, T. *et al.* Sensor histidine kinases mediate ABA and osmostress signaling in the moss Physcomitrium patens. *Curr Biol* **32**, 164-175 e168 (2022). https://doi.org:10.1016/j.cub.2021.10.068

69 Song, Z. T., Zhang, L. L., Han, J. J., Zhou, M. & Liu, J. X. Histone H3K4 methyltransferases SDG25 and ATX1 maintain heat-stress gene expression during recovery in Arabidopsis. *Plant J* **105**, 1326-1338 (2021). https://doi.org:10.1111/tpj.15114

70 Meng, X. & Zhang, S. MAPK cascades in plant disease resistance signaling. *Annu Rev Phytopathol* **51**, 245-266 (2013). https://doi.org:10.1146/annurev-phyto-082712-102314

71 Hohmann, U., Lau, K. & Hothorn, M. The Structural Basis of Ligand Perception and Signal Activation by Receptor Kinases. *Annu Rev Plant Biol* **68**, 109-137 (2017). https://doi.org:10.1146/annurev-arplant-042916-040957

72 Hoang, X. L. T. *et al.* Histidine Kinases: Diverse Functions in Plant Development and Responses to Environmental Conditions. *Annu Rev Plant Biol* **72**, 297-323 (2021). https://doi.org:10.1146/annurev-arplant-080720-093057

73 Dievart, A., Gottin, C., Perin, C., Ranwez, V. & Chantret, N. Origin and Diversity of Plant Receptor-Like Kinases. *Annu Rev Plant Biol* **71**, 131-156 (2020). https://doi.org:10.1146/annurev-arplant-073019-025927

74 Meyer, H. M., Hotta, T., Malkovskiy, A., Zheng, Y. & Ehrhardt, D. W. (2023). https://doi.org:10.1101/2023.11.01.565081

75 Dai, S. *et al.* BROTHER OF LUX ARRHYTHMO is a component of the Arabidopsis circadian clock. *Plant Cell* **23**, 961-972 (2011). https://doi.org:10.1105/tpc.111.084293

76 Shi, L., Wu, Y. & Sheen, J. TOR signaling in plants: conservation and innovation. *Development* **145** (2018). https://doi.org:10.1242/dev.160887

77 Burkart, G. M. & Brandizzi, F. A Tour of TOR Complex Signaling in Plants. *Trends Biochem Sci* **46**, 417-428 (2021). https://doi.org:10.1016/j.tibs.2020.11.004

78 Uhrig, R. G., Labandera, A. M. & Moorhead, G. B. Arabidopsis PPP family of serine/threonine protein phosphatases: many targets but few engines. *Trends Plant Sci* **18**, 505-513 (2013). https://doi.org:10.1016/j.tplants.2013.05.004

79 Kieber, J. J. & Schaller, G. E. Cytokinin signaling in plant development. *Development* **145** (2018). https://doi.org:10.1242/dev.149344

80 Schroder, F., Lisso, J., Lange, P. & Mussig, C. The extracellular EXO protein mediates cell expansion in Arabidopsis leaves. *BMC Plant Biol* **9**, 20 (2009). https://doi.org:10.1186/1471-2229-9-20

81 Meteignier, L. V. *et al.* The Arabidopsis mTERF-repeat MDA1 protein plays a dual function in transcription and stabilization of specific chloroplast transcripts within the psbE and ndhH operons. *New Phytol* **227**, 1376-1391 (2020). https://doi.org:10.1111/nph.16625

82 Hammani, K. & Barkan, A. An mTERF domain protein functions in group II intron splicing in maize chloroplasts. *Nucleic Acids Res* **42**, 5033-5042 (2014). https://doi.org:10.1093/nar/gku112

83 Sun, X., Xu, D., Liu, Z., Kleine, T. & Leister, D. Functional relationship between mTERF4 and GUN1 in retrograde signaling. *J Exp Bot* **67**, 3909-3924 (2016). https://doi.org:10.1093/jxb/erv525

84 Rieseberg, T. P. *et al.* Crossroads in the evolution of plant specialized metabolism. *Semin Cell Dev Biol* **134**, 37-58 (2023). https://doi.org:10.1016/j.semcdb.2022.03.004

85 Chen, X. *et al.* Protein kinases in plant responses to drought, salt, and cold stress. *J Integr Plant Biol* **63**, 53-78 (2021). https://doi.org:10.1111/jipb.13061

86 Rieseberg, T. P. *et al.* Divergent responses in desiccation experiments in two ecophysiologically different Zygnematophyceae. *Physiol Plant* **175**, e14056 (2023). https://doi.org:10.1111/ppl.14056

87 Nichols, H. *Handbook of Phycological Methods*. 16-17 (Cambridge University Press, 1973).

88 Ashton, N. W. & Cove, D. J. The isolation and preliminary characterisation of auxotrophic and analogue resistant mutants of the moss, Physcomitrella patens. *Molecular and General Genetics MGG* **154**, 87-95 (1977). https://doi.org:10.1007/bf00265581

89 Aronsson, H. *et al.* Monogalactosyldiacylglycerol deficiency in Arabidopsis affects pigment composition in the prolamellar body and impairs thylakoid membrane energization and photoprotection in leaves. *Plant Physiol* **148**, 580-592 (2008). https://doi.org:10.1104/pp.108.123372

90 Gupta, P., Sreelakshmi, Y. & Sharma, R. A rapid and sensitive method for determination of carotenoids in plant tissues by high performance liquid chromatography. *Plant Methods* **11**, 5 (2015). https://doi.org:10.1186/s13007-015-0051-0

91 Lin, C. H. & Chen, B. H. Determination of carotenoids in tomato juice by liquid chromatography. *J Chromatogr A* **1012**, 103-109 (2003). https://doi.org:10.1016/s0021-9673(03)01138-5

92 Thrane, J. E. *et al.* Spectrophotometric Analysis of Pigments: A Critical Assessment of a High-Throughput Method for Analysis of Algal Pigment Mixtures by Spectral Deconvolution. *PLoS One* **10**, e0137645 (2015). https://doi.org:10.1371/journal.pone.0137645

93 Rivers, J. Y., Truong, T. T., Pogson, B. J. & McQuinn, R. P. Volatile apocarotenoid discovery and quantification in Arabidopsis thaliana: optimized sensitive analysis via HS-SPME-GC/MS. *Metabolomics* **15**, 79 (2019). https://doi.org:10.1007/s11306-019-1529-y

94 Jones, P. *et al.* InterProScan 5: genome-scale protein function classification. *Bioinformatics* **30**, 1236-1240 (2014). https://doi.org:10.1093/bioinformatics/btu031

95 Buchfink, B., Reuter, K. & Drost, H.-G. Sensitive protein alignments at tree-of-life scale using DIAMOND. *Nat Methods* **18**, 366-368 (2021). https://doi.org:10.1038/s41592-021-01101-x

96 Cantalapiedra, C. P., Hernández-Plaza, A., Letunic, I., Bork, P. & Huerta-Cepas, J. eggNOG-mapper v2: Functional Annotation, Orthology Assignments, and Domain Prediction at the Metagenomic Scale. (Bioinformatics, 2021).

97 Huerta-Cepas, J. *et al.* eggNOG 5.0: a hierarchical, functionally and phylogenetically annotated orthology resource based on 5090 organisms and 2502 viruses. *Nucleic Acids Research* **47**, D309-D314 (2019). https://doi.org:10.1093/nar/gky1085

98 Camacho, C. *et al.* BLAST+: architecture and applications. *BMC Bioinformatics* **10**, 421 (2009). https://doi.org:10.1186/1471-2105-10-421

99 Cheng, C. Y. *et al.* Araport11: a complete reannotation of the *Arabidopsis thaliana* reference genome. *The Plant Journal* **89**, 789-804 (2017). https://doi.org:10.1111/tpj.13415

100 Emms, D. M. & Kelly, S. OrthoFinder: solving fundamental biases in whole genome comparisons dramatically improves orthogroup inference accuracy. *Genome Biol* **16**, 157 (2015). https://doi.org:10.1186/s13059-015-0721-2

101 Emms, D. M. & Kelly, S. OrthoFinder: phylogenetic orthology inference for comparative genomics. *Genome Biol* **20**, 238 (2019). https://doi.org:10.1186/s13059-019-1832-y

102 Katoh, K. & Standley, D. M. MAFFT Multiple Sequence Alignment Software Version 7: Improvements in Performance and Usability. *Molecular Biology and Evolution* **30**, 772-780 (2013). https://doi.org:10.1093/molbev/mst010

103 Price, M. N., Dehal, P. S. & Arkin, A. P. FastTree 2 – Approximately Maximum-Likelihood Trees for Large Alignments. *PLoS ONE* **5**, e9490 (2010). https://doi.org:10.1371/journal.pone.0009490

104 Li, F.-W. *et al.* Anthoceros genomes illuminate the origin of land plants and the unique biology of hornworts. *Nature Plants* **6**, 259-272 (2020). https://doi.org:10.1038/s41477-020-0618-2

105 Li, F.-W. *et al.* Fern genomes elucidate land plant evolution and cyanobacterial symbioses. *Nature Plants* **4**, 460-472 (2018). https://doi.org:10.1038/s41477-018-0188-8

106 The International Brachypodium, I. Genome sequencing and analysis of the model grass Brachypodium distachyon. *Nature* **463**, 763-768 (2010). https://doi.org:10.1038/nature08747

107 Irisarri, I. *et al.* Unexpected cryptic species among streptophyte algae most distant to land plants. *Proc Biol Sci* **288**, 20212168 (2021). https://doi.org:10.1098/rspb.2021.2168

108 Merchant, S. S. *et al.* The *Chlamydomonas* Genome Reveals the Evolution of Key Animal and Plant Functions. *Science* **318**, 245-250 (2007). https://doi.org:10.1126/science.1143609

109 Sekimoto, H. *et al.* A divergent RWP-RK transcription factor determines mating type in heterothallic Closterium. *New Phytologist* **237**, 1636-1651 (2023). https://doi.org:10.1111/nph.18662

110 Montgomery, S. A. *et al.* Chromatin Organization in Early Land Plants Reveals an Ancestral Association between H3K27me3, Transposons, and Constitutive Heterochromatin. *Current Biology* **30**, 573-588.e577 (2020). https://doi.org:10.1016/j.cub.2019.12.015

111 Cheng, S. *et al.* Genomes of Subaerial Zygnematophyceae Provide Insights into Land Plant Evolution. *Cell* **179**, 1057-1067.e1014 (2019). https://doi.org:10.1016/j.cell.2019.10.019

112 Palenik, B. *et al.* The tiny eukaryote *Ostreococcus* provides genomic insights into the paradox of plankton speciation. *Proc. Natl. Acad. Sci. U.S.A.* **104**, 7705-7710 (2007). https://doi.org:10.1073/pnas.0611046104

113 Ouyang, S. *et al.* The TIGR Rice Genome Annotation Resource: improvements and new features. *Nucleic Acids Research* **35**, D883-D887 (2007). https://doi.org:10.1093/nar/gkl976

114 Li, L. *et al.* The genome of Prasinoderma coloniale unveils the existence of a third phylum within green plants. *Nat Ecol Evol* **4**, 1220-1231 (2020). https://doi.org:10.1038/s41559-020-1221-7

115 Jiao, C. *et al.* The Penium margaritaceum Genome: Hallmarks of the Origins of Land Plants. *Cell* **181**, 1097-1111.e1012 (2020). https://doi.org:10.1016/j.cell.2020.04.019

116 The Tomato Genome, C. The tomato genome sequence provides insights into fleshy fruit evolution. *Nature* **485**, 635-641 (2012). https://doi.org:10.1038/nature11119

117 Banks, J. A. *et al.* The Selaginella Genome Identifies Genetic Changes Associated with the Evolution of Vascular Plants. *Science* **332**, 960-963 (2011). https://doi.org:10.1126/science.1203810

118 Jiao, Y. *et al.* Improved maize reference genome with single-molecule technologies. *Nature* **546**, 524-527 (2017). https://doi.org:10.1038/nature22971

119 Greene, D., Richardson, S. & Turro, E. ontologyX: a suite of R packages for working with ontological data. *Bioinformatics* **33**, 1104-1106 (2017). https://doi.org:10.1093/bioinformatics/btw763

120 Wilhelmsson, P. K. I., Mühlich, C., Ullrich, K. K. & Rensing, S. A. Comprehensive Genome-Wide Classification Reveals That Many Plant-Specific Transcription Factors Evolved in Streptophyte Algae. *Genome Biology and Evolution* **9**, 3384-3397 (2017). https://doi.org:10.1093/gbe/evx258

121 Mölder, F. *et al.* Sustainable data analysis with Snakemake. *F1000Res* **10**, 33 (2021). https://doi.org:10.12688/f1000research.29032.1

122 Andrews, S. (Babraham Bioinformatics, Babraham Institute, Cambridge, United Kingdom, 2010).

123 Ewels, P., Magnusson, M., Lundin, S. & Käller, M. MultiQC: summarize analysis results for multiple tools and samples in a single report. *Bioinformatics* **32**, 3047-3048 (2016). https://doi.org:10.1093/bioinformatics/btw354

124 Bolger, A. M., Lohse, M. & Usadel, B. Trimmomatic: a flexible trimmer for Illumina sequence data. *Bioinformatics* **30**, 2114-2120 (2014). https://doi.org:10.1093/bioinformatics/btu170

125 Bray, N. L., Pimentel, H., Melsted, P. & Pachter, L. Near-optimal probabilistic RNA-seq quantification. *Nat Biotechnol* **34**, 525-527 (2016). https://doi.org:10.1038/nbt.3519

126 R Core Team, A. & Team, R. C. (2022).

127 Wickham, H. *et al.* Welcome to the Tidyverse. *Journal of open source software* **4**, 1686 (2019).

128 Soneson, C., Love, M. I. & Robinson, M. D. Differential analyses for RNA-seq: transcript-level estimates improve gene-level inferences. *F1000Res* **4** (2015).

129 Robinson, M. D., McCarthy, D. J. & Smyth, G. K. edgeR: a Bioconductor package for differential expression analysis of digital gene expression data. *bioinformatics* **26**, 139-140 (2010).

130 Hicks, S. C. & Irizarry, R. A. Quantro: a data-driven approach to guide the choice of an appropriate normalization method. *Genome Biol* **16**, 1-8 (2015).

131 Hicks, S. C. *et al.* Smooth quantile normalization. *Biostatistics* **19**, 185-198 (2018).

132 Ritchie, M. E. *et al.* limma powers differential expression analyses for RNA-sequencing and microarray studies. *Nucleic Acids Research* **43**, e47-e47 (2015).

133 Wu, T. *et al.* clusterProfiler 4.0: A universal enrichment tool for interpreting omics data. *The innovation* **2** (2021).

134 Brunson, J. C. Ggalluvial: layered grammar for alluvial plots. *Journal of Open Source Software* **5** (2020).

135 Chowdhury, H. A., Bhattacharyya, D. K. & Kalita, J. K. (Differential) co-expression analysis of gene expression: a survey of best practices. *IEEE/ACM transactions on computational biology and bioinformatics* **17**, 1154-1173 (2019).

136 Langfelder, P. & Horvath, S. WGCNA: an R package for weighted correlation network analysis. *BMC Bioinformatics* **9**, 1-13 (2008).

137 Csardi, G. & Nepusz, T. The igraph software package for complex network research. *InterJournal, complex systems* **1695**, 1-9 (2006).

138 Lu, J. *et al.* Causal network inference from gene transcriptional time-series response to glucocorticoids. *PLoS computational biology* **17**, e1008223 (2021).

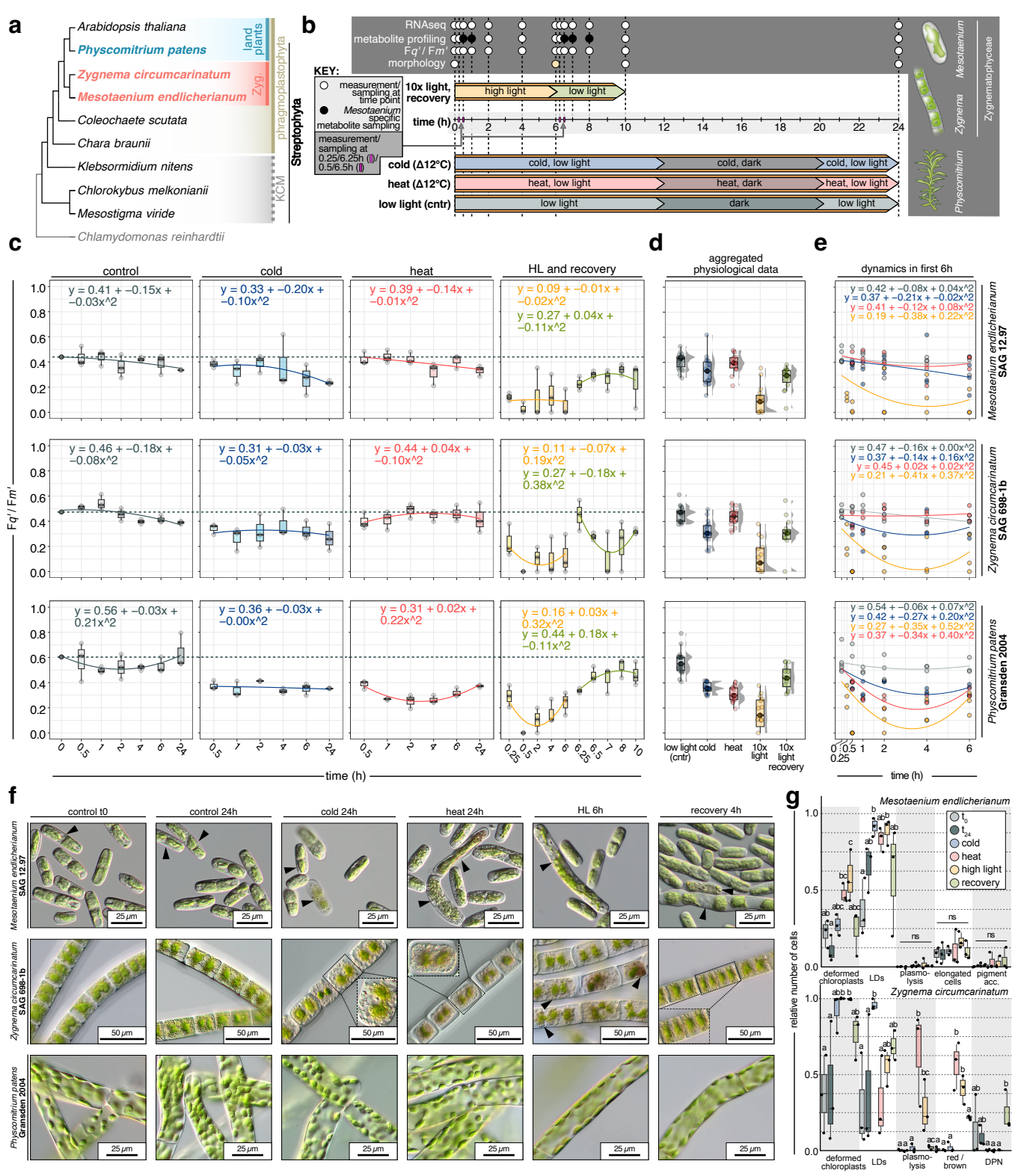
a
Arabidopsis thaliana
Physcomitrium patens
Zygnema circumcarinatum
Mesotaenium endlicherianum
Coleochaete scutata
Chara braunii
Klebsormidium nitens
Chlorokybus melkonianii
Mesostigma viride
Chlamydomonas reinhardtii
land plants
Zyg.
phragmoplastophyta
KOM
Streptophyta
b
RNAseq
metabolite profiling
Fq′/ Fm′
morphology
KEY:
measurement/ sampling at time point
Mesotaenium specific metabolite sampling
measurement/ sampling at 0.25/6.25h / 0.5/6.5h
10x light, recovery
high light
low light
time (h)
cold (Δ12°C)
cold, low light
cold, dark
cold, low light
heat (Δ12°C)
heat, low light
heat, dark
heat, low light
low light (cntr)
low light
dark
low light
Mesotaenium
Zygnema
Physcomitrium
Zygnematophyceae
c
control
cold
heat
HL and recovery
Fq′/ Fm′
time (h)
d
aggregated physiological data
low light (cntr)
cold
heat
10x light
10x light recovery
e
dynamics in first 6h
time (h)
Mesotaenium endlicherianum SAG 12.97
Zygnema circumcarinatum SAG 698-1b
Physcomitrium patens Gransden 2004
f
control t0
control 24h
cold 24h
heat 24h
HL 6h
recovery 4h
25 µm
50 µm
g
Mesotaenium endlicherianum
Zygnema circumcarinatum
relative number of cells
deformed chloroplasts
LDs
plasmo-lysis
elongated cells
pigment acc.
red / brown
DPN
ns
cold
heat
high light
recovery

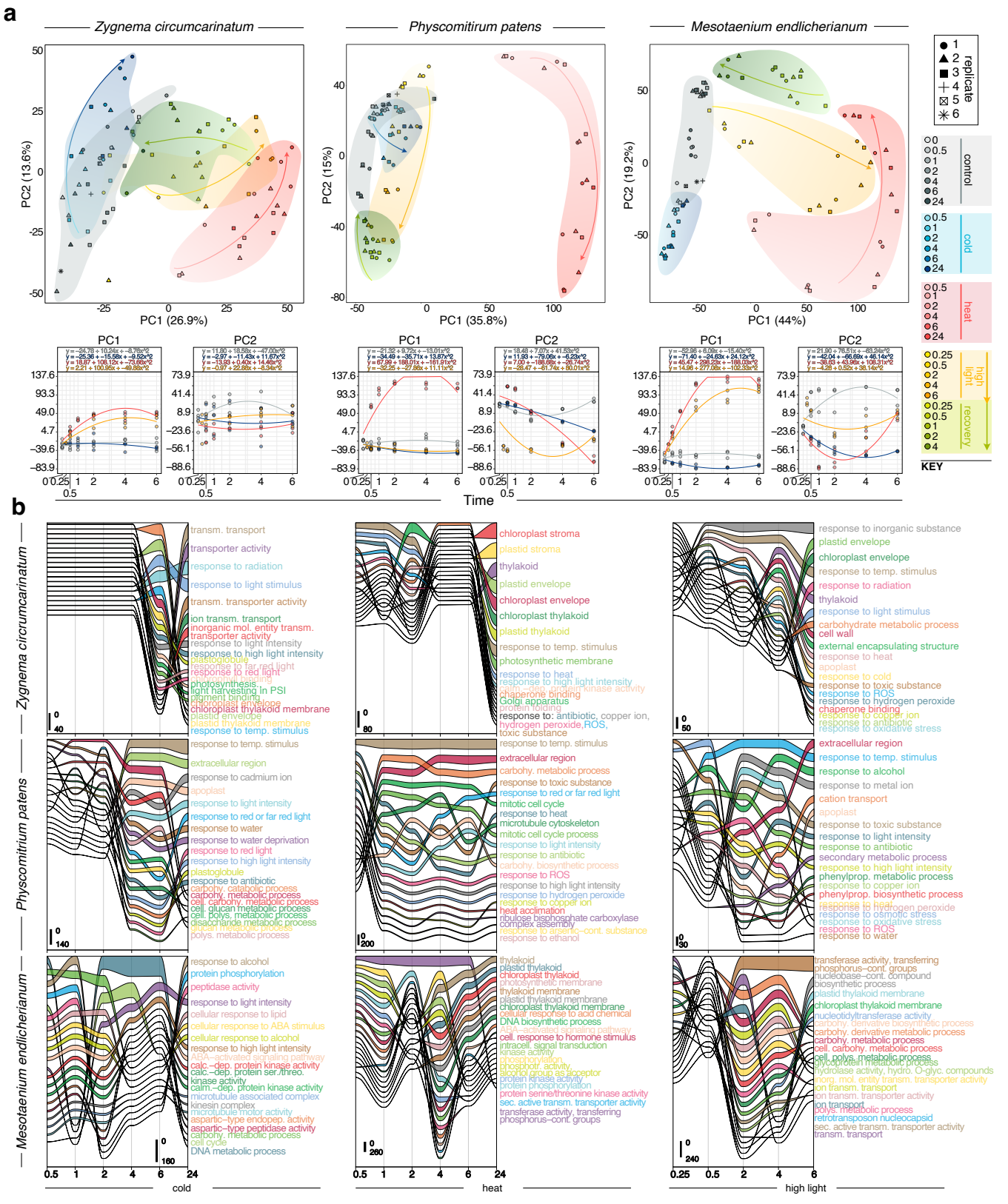
a
Zygnema circumcarinatum
Physcomitirum patens
Mesotaenium endlicherianum
PC2 (13.6%)
PC1 (26.9%)
PC2 (15%)
PC1 (35.8%)
PC2 (19.2%)
PC1 (44%)
replicate
control
cold
heat
high light
recovery
KEY
PC1
PC2
Time
b
Zygnema circumcarinatum
Physcomitirum patens
Mesotaenium endlicherianum
cold
heat
high light

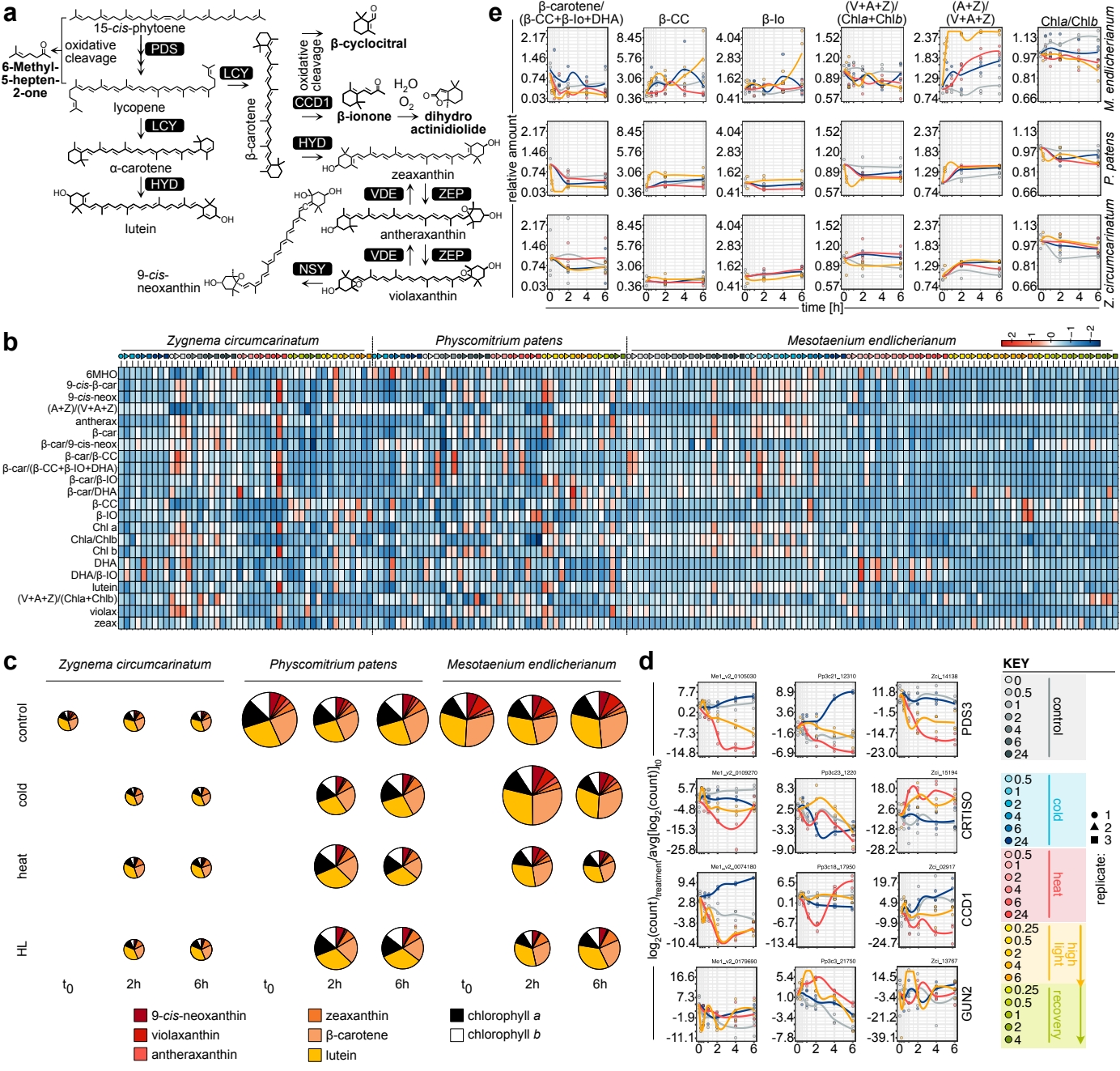
a
15-cis-phytoene
PDS
6-Methyl-5-hepten-2-one
oxidative cleavage
lycopene
LCY
LCY
α-carotene
HYD
lutein
β-carotene
oxidative cleavage
β-cyclocitral
CCD1
β-ionone
H2O
O2
dihydro actinidiolide
HYD
zeaxanthin
VDE
ZEP
antheraxanthin
VDE
ZEP
violaxanthin
NSY
9-cis-neoxanthin
e
β-carotene/(β-CC+β-Io+DHA)
β-CC
β-Io
(V+A+Z)/(Chla+Chlb)
(A+Z)/(V+A+Z)
Chla/Chlb
relative amount
M. endlicherianum
P. patens
Z. circumcarinatum
time [h]
b
Zygnema circumcarinatum
Physcomitrium patens
Mesotaenium endlicherianum
6MHO
9-cis-β-car
9-cis-neox
(A+Z)/(V+A+Z)
antherax
β-car
β-car/9-cis-neox
β-car/β-CC
β-car/(β-CC+β-IO+DHA)
β-car/β-IO
β-car/DHA
β-CC
β-IO
Chl a
Chla/Chlb
Chl b
DHA
DHA/β-IO
lutein
(V+A+Z)/(Chla+Chlb)
violax
zeax
c
Zygnema circumcarinatum
Physcomitrium patens
Mesotaenium endlicherianum
control
cold
heat
HL
t0
2h
6h
9-cis-neoxanthin
violaxanthin
antheraxanthin
zeaxanthin
β-carotene
lutein
chlorophyll a
chlorophyll b
d
log2(count)treatment /avg[log2(count)]40
PDS3
CRTISO
CCD1
GUN2
KEY
control
cold
heat
high light
recovery
replicate:

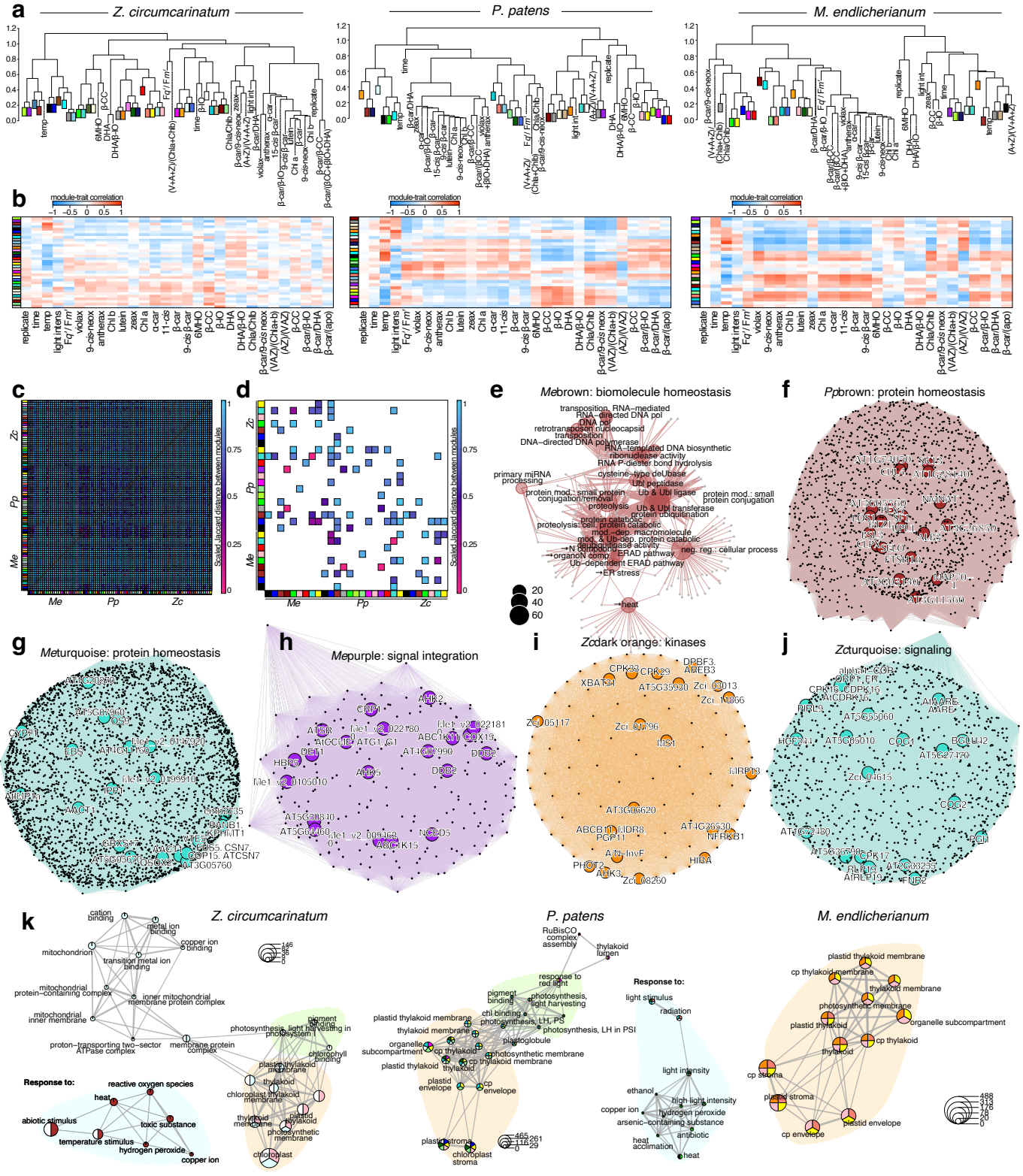
a
Z. circumcarinatum
P. patens
M. endlicherianum
b
module-trait correlation
c
d
Scaled Jaccard distance between modules
e
Mebrown: biomolecule homeostasis
f
Ppbrown: protein homeostasis
g
Meturquoise: protein homeostasis
h
Mepurple: signal integration
i
Zcdark orange: kinases
j
Zcturquoise: signaling
k
Z. circumcarinatum
P. patens
M. endlicherianum
Response to:

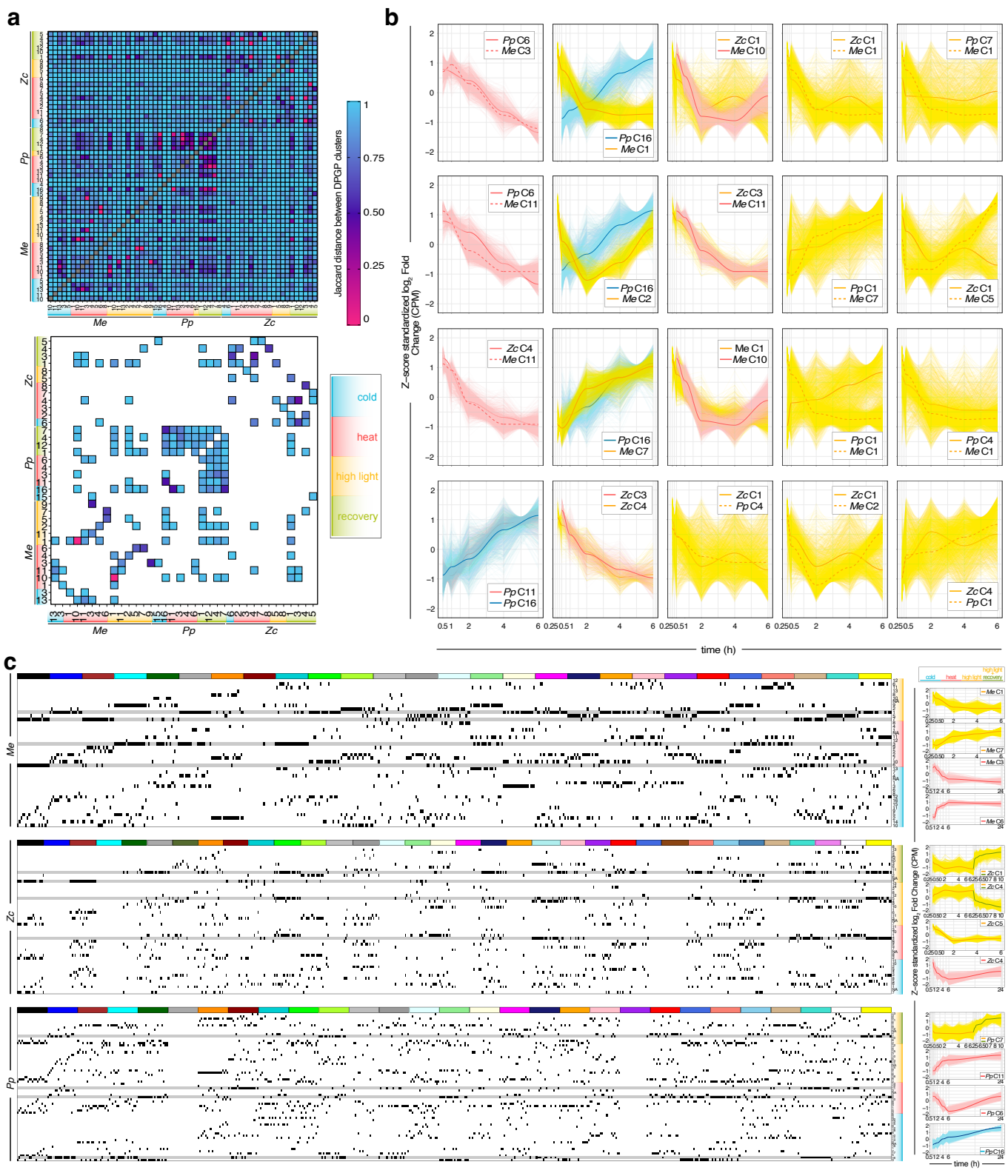
a
Zc
Pp
Me
Jaccard distance between DPGP clusters
1
0.75
0.50
0.25
0
cold
heat
high light
recovery
b
Z-score standardized log2 Fold Change (CPM)
Pp C6
Me C3
Pp C16
Me C1
Zc C1
Me C10
Zc C1
Me C1
Pp C7
Me C1
Pp C6
Me C11
Pp C16
Me C2
Zc C3
Me C11
Pp C1
Me C7
Zc C1
Me C5
Zc C4
Me C11
Pp C16
Me C7
Me C1
Me C10
Pp C1
Me C1
Pp C4
Me C1
Pp C11
Pp C16
Zc C3
Zc C4
Zc C1
Pp C4
Zc C1
Me C2
Zc C4
Pp C1
time (h)
c
Me
Zc
Pp
time (h)

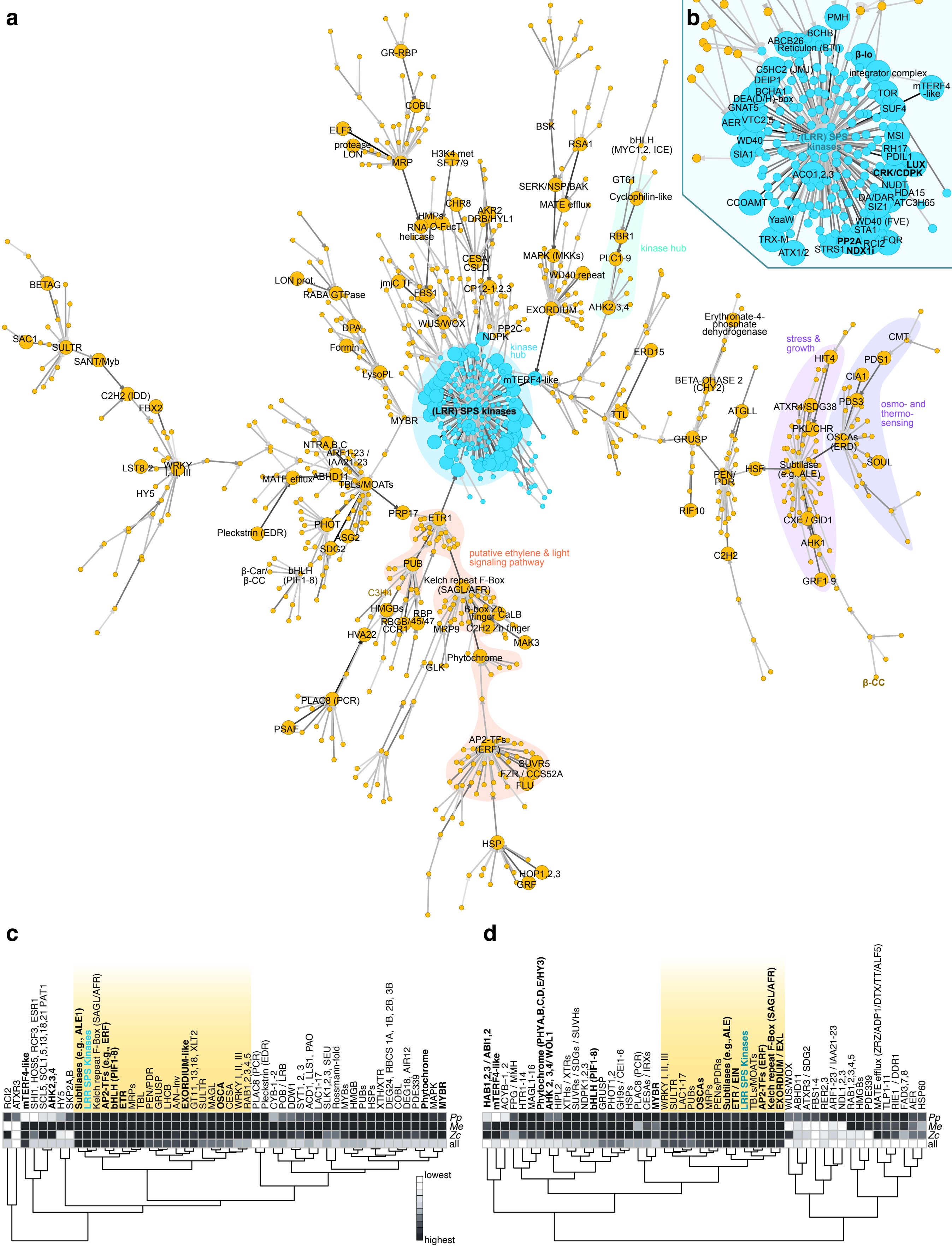
a
b
c
d
kinase hub
putative ethylene & light signaling pathway
stress & growth
osmo- and thermo-sensing
(LRR) SPS kinases
lowest
highest